ACS NANO
www.acsnano.org

Low-Frequency Shear and Layer-Breathing Modes in Raman Scattering of Two-Dimensional Materials

Liangbo Liang,[†,⊥] Jun Zhang,[‡,¶,⊥] Bobby G. Sumpter,[†,§] Qing-Hai Tan,[‡,¶] Ping-Heng Tan,[*,‡,¶] and Vincent Meunier[*,∥]

[†]Center for Nanophase Materials Sciences, Oak Ridge National Laboratory, Oak Ridge, Tennessee 37831, United States
[‡]State Key Laboratory of Superlattices and Microstructures, Institute of Semiconductors, Chinese Academy of Sciences, Beijing 100083, China
[¶]CAS Center of Excellence in Topological Quantum Computation, University of Chinese Academy of Sciences, Beijing 100190, China
[§]Computational Sciences and Engineering Division, Oak Ridge National Laboratory, Oak Ridge, Tennessee 37831, United States
[∥]Department of Physics, Applied Physics, and Astronomy, Rensselaer Polytechnic Institute, Troy, New York 12180, United States

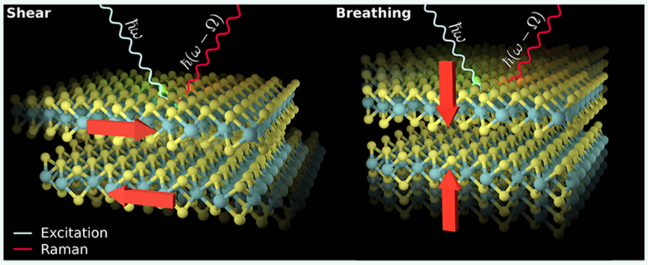

ABSTRACT: Ever since the isolation of single-layer graphene in 2004, two-dimensional layered structures have been among the most extensively studied classes of materials. To date, the pool of two-dimensional materials (2DMs) continues to grow at an accelerated pace and already covers an extensive range of fascinating and technologically relevant properties. An array of experimental techniques have been developed and used to characterize and understand these properties. In particular, Raman spectroscopy has proven to be a key experimental technique, thanks to its capability to identify minute structural and electronic effects in nondestructive measurements. While high-frequency (HF) intralayer Raman modes have been extensively employed for 2DMs, recent experimental and theoretical progress has demonstrated that low-frequency (LF) interlayer Raman modes are more effective at determining layer numbers and stacking configurations and provide a unique opportunity to study interlayer coupling. These advantages are due to 2DMs' unique interlayer vibration patterns where each layer behaves as an almost rigidly moving object with restoring forces corresponding to weak interlayer interactions. Compared to HF Raman modes, the relatively small attention originally devoted to LF Raman modes is largely due to their weaker signal and their proximity to the strong Rayleigh line background, which previously made their detection challenging. Recent progress in Raman spectroscopy with technical and hardware upgrades now makes it possible to probe LF modes with a standard single-stage Raman system and has proven crucial to characterize and understand properties of 2DMs. Here, we present a comprehensive and forward-looking review on the current status of exploiting LF Raman modes of 2DMs from both experimental and theoretical perspectives, revealing the fundamental physics and technological significance of LF Raman modes in advancing the field of 2DMs. We review a broad array of materials, with varying thickness and stacking configurations, discuss the effect of in-plane anisotropy, and present a generalized linear chain model and interlayer bond polarizability model to rationalize the experimental findings. We also discuss the instrumental improvements of Raman spectroscopy to enhance and separate LF Raman signals from the Rayleigh line. Finally, we highlight the opportunities and challenges ahead in this fast-developing field.

KEYWORDS: *two-dimensional materials, Raman scattering, low-frequency phonons, interlayer vibrations, interlayer coupling, thickness fingerprints, stacking fingerprints, linear chain model, interlayer bond polarizability model*

The discovery of graphene marked the beginning of an era of tremendous interest in two-dimensional layered materials. Now, the field has developed into a diverse and still growing family of two-dimensional materials (2DMs), ranging from insulators (h-BN, *etc.*), topological insulators (Bi_2Se_3, Bi_2Te_3, *etc.*), semiconductors (MoS_2, $MoSe_2$, WS_2,

Received: September 14, 2017
Accepted: November 3, 2017
Published: November 3, 2017

DOI: 10.1021/acsnano.7b06551
ACS Nano 2017, 11, 11777−11802

WSe_2, ReS_2, $ReSe_2$, $PdSe_2$, GaS, GaSe, GeSe, SnS, phosphorene, *etc.*), semimetals (graphene, $NiTe_2$, *etc.*), to superconductors (NbS_2, $NbSe_2$, $TaSe_2$, FeSe, FeTe, *etc.*).[1−13] After intensive investigations of graphene and transition-metal dichalcogenides (TMDCs) like MoS_2, other layered structures, such as black phosphorus (or phosphorene, in the single layer limit), have more recently joined the array of 2DMs with promising potential for nanoelectronics, optoelectronics, and thermal applications.[14−21] In addition, many 2DMs that had been initially considered to exist only in the realm of theorists' imagination have now been synthesized, including silicene,[22−25] germanene,[26−28] stanene,[29] and borophene.[30]

In 2DMs, the atoms within each layer are connected by covalent or ionic bonds, while generally weak van der Waals (vdW) interactions hold the layers together. Subsequently, the layers can be separated into building blocks and reassembled either horizontally or vertically to form heterostructures. These heterostructures can either feature the combined functionality of the individual layers or even lead to emergent properties,[5,9,11,31] such as semiconductor p−n heterojunctions for photodetection and solar energy harvesting.[32−35] Based on these recent developments, it would seem that the diversity of 2DMs could offer limitless combinations of heterostructures and heterojunctions, for the assembly of functional materials-by-design.

The properties of 2DMs can be understood as the combination of properties of individual layers, their structural symmetry, and the interlayer coupling. The latter is very sensitive to the number of layers in the stack and the details of the stacking, such as relative registry and twisting angle. Consequently, functionality can in principle be tuned and optimized by changing the material's thickness and stacking. The properties of multilayer 2DMs depend critically on the number of layers (N).[7] For instance, bulk MoS_2 has an indirect electronic bandgap, but in the single-layer realization of MoS_2, a transition from indirect to direct bandgap occurs, together with a strong enhancement of photoluminescence (PL).[36,37] As another illustration of an N-dependent property, black phosphorus (BP) has an intrinsic thickness-dependent direct bandgap (ranging from 0.3 eV for the bulk to 2.0 eV for a monolayer), a property that promises a broad range of optoelectronic applications.[14,15,18,38] Furthermore, manipulating stacking order is another powerful approach to tailor 2DMs and their heterostructures for electronic and optoelectronic applications. For instance, in twisted or stacked graphene layers, minute changes in stacking can lead to large-period Moiré superlattices accompanied by unusual behaviors and phenomena, such as fractional quantum Hall effects, the appearance of stacking-dependent Van Hove singularities near the Fermi energy, among others.[39−43] Trilayer graphene is commonly found in two low-energy stacking patterns, known as ABA (Bernal) and ABC (rhombohedral), which exhibit distinct electronic properties owing to the stacking-dependent electronic interactions and symmetries.[44−47] In bilayer MoS_2, proper manipulation of stacking orders can break the inversion symmetry, evoking strong valley and spin polarization that cannot be achieved in natural 2H-stacked bilayers.[42] Furthermore, the recently observed spin/valley polarization in symmetry-breaking 3R-stacked MoS_2 further highlights the key role of stacking sequences in the properties of 2DMs.[48] For twisted bilayer MoS_2, the electronic structures and exciton/trion behaviors can be fine-tuned by changing the interlayer twisting angle.[49−51] Clearly these few selected examples illustrate the important need for a precise characterization of the stacking order and an accurate determination of the number of layers for future developments of 2DMs.

Characterization of two-dimensional crystals has been based on a large variety of electron microscopy, atomic force microscopy (AFM), and optical spectroscopy methods.[52,53] Among them, Raman spectroscopy stands out since it is a fast, nondestructive, and relatively inexpensive tool with high spectral resolution that provides structural and electronic information at both laboratory and mass-production scales.[10−12,31] In addition to being an excellent probe for material quality, it has been used in 2DMs in an effort to enable rapid identification of the material's thickness and stacking order. Initially, the majority of research activities focused on analyzing high-frequency (HF) modes, which involve vibrations stemming from the intralayer chemical bonds.[10,12,31,54,55] In these modes, conventionally called *intralayer modes*, the restoring forces are dominated by the strength of the intralayer chemical bonds rather than those holding the layers together, which are typically of vdW type. Consequently, HF intralayer modes are not very sensitive to the interlayer coupling, and there are great limitations associated with their use as a general approach for the unambiguous determination of thickness and stacking order. In stark contrast, low-frequency (LF) *interlayer modes* correspond to layer−layer vibrations where each layer moves nearly rigidly as a whole unit. It follows that the corresponding frequencies are almost solely determined by the interlayer restoring forces. The weak nature of layer−layer interactions, in addition to the fact that a large ensemble of atoms move together, typically yields frequencies well below 100 cm^{-1} and are thus usually observed, in Raman spectroscopy, close to the strong Rayleigh line.[9,11,56] These LF modes are categorized into two types: in-plane shear and out-of-plane breathing vibration modes. Due to their greater sensitivity to interlayer coupling, LF Raman modes have recently started to attract increasing attention as highly sensitive probes of interfacial coupling, including coupling to a substrate. One of the pioneering works in this area was performed by Tan *et al.* in 2012 who characterized multilayer graphene (MLG) samples.[57] Since then, a fast growing number of publications have demonstrated LF Raman modes as effective indicators of the layer thickness[19,57−72] and stacking order[52,73−81] in a broad variety of 2DMs. Furthermore, LF Raman modes have also been extended to investigate the interfacial coupling and stacking configurations in twisted two-dimensional homostructures and heterostructures, such as twisted MLG,[43,82,83] twisted bilayer TMDCs,[84,85] and TMDCs heterostructures.[86,87] Based on these reports, it is clear that the measurement of LF interlayer vibrational modes by Raman spectroscopy is becoming increasingly important and useful in characterizing two-dimensional layered materials and the associated vdW heterostructures.

The objective of this review is to present a comprehensive, state-of-the-art, and forward-looking account of the use of LF Raman spectroscopy in 2DMs from both experimental and theoretical perspectives. First, we discuss general properties of interlayer vibration modes in 2DMs and how they can be understood from group theory and the linear chain model (LCM). Second, we describe the LF Raman scattering technique and recent upgrades for improved detection of LF Raman signals. Third, we summarize the recent advances on using LF Raman modes for the thickness and stacking determination of diverse 2DMs. We show that the simple

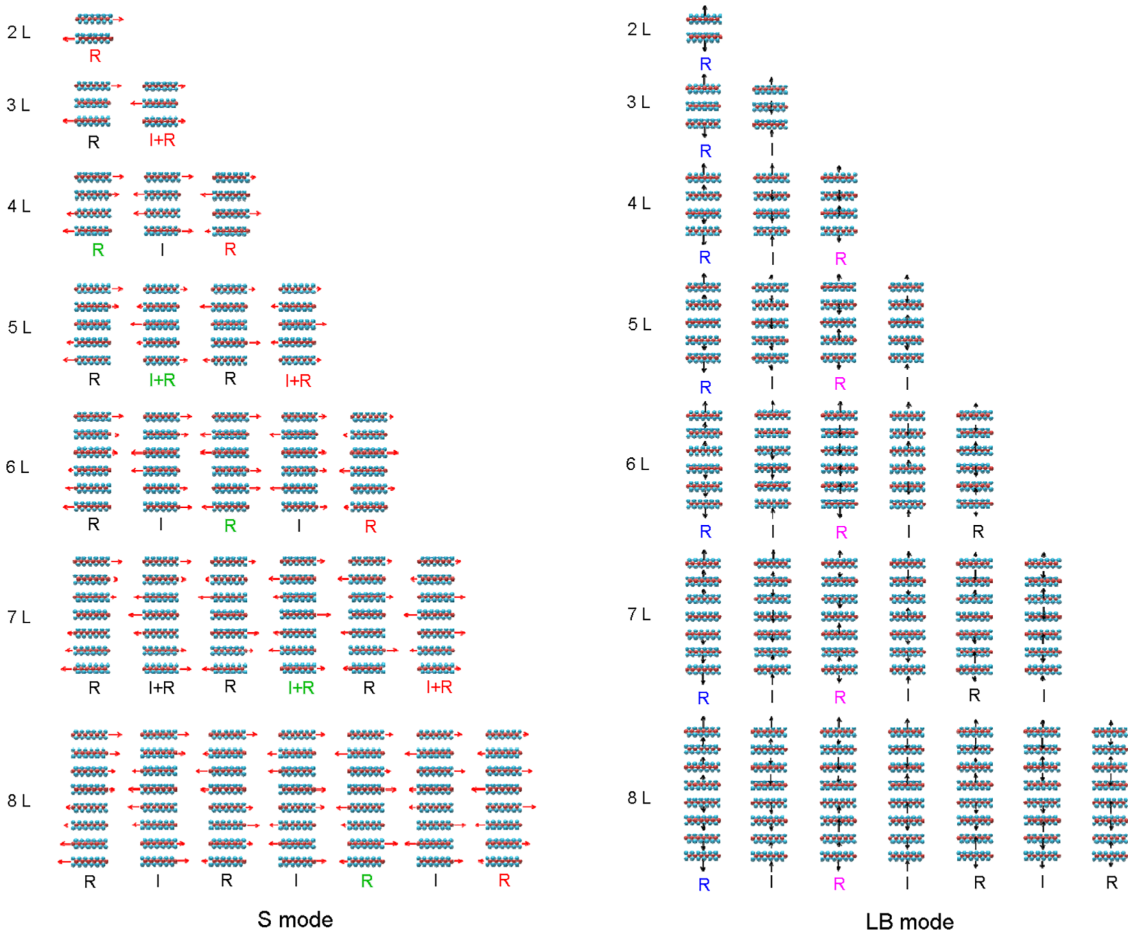

Figure 1. Schematic of interlayer shear and layer-breathing modes in 2−8L TMDCs like MoS_2. Both shear and layer-breathing modes are ordered from low to high frequency, from left to right. The arrows indicate the vibrations of each rigid layer. The Raman/infrared activity is listed below the vibrations for TMDCs in 2H phase. Adapted with permission from ref 64. Copyright 2013 American Chemical Society.

LCM and interlayer bond polarizability model, together with first-principles methods, can be adopted to understand the thickness and stacking dependence of LF modes, respectively. Fourth, we briefly discuss the latest LF Raman studies on two-dimensional heterostructures. Finally, we highlight the opportunities and challenges ahead in this fast-developing field from both experimental and theoretical points of view.

PROPERTIES OF INTERLAYER SHEAR AND LAYER-BREATHING MODES

Vibration, Symmetry, Raman Activity, And Polarization Dependence of Interlayer Modes. Similar to other materials, whether a lattice vibration mode in a 2DM can be experimentally observed or not in a Raman measurement is determined by the symmetry of the crystal. Conversely, the actual phonon frequency of each mode is dictated by the details of the chemical and physical atomic bonding. Understanding the LF vibration modes that are Raman active first requires an exhaustive analysis of their lattice symmetry.[11,64] Because group theory formally transforms complex symmetry operations into simple linear algebraic relations, it provides a fundamental mathematical framework to understand phonon properties from the crystal symmetry. The LF vibration modes represent relative motions between rigid monolayer planes when assembled in *N*-layer stacks. In this review, we will refer to a system by its chemical formula preceded by the label "*N*L" (*e.g.*, trilayer MoS_2 is referred to 3L MoS_2) with additional labels included to specify stacking symmetry, when appropriate.

We will first focus on TMDCs and in particular on the in-plane isotropic 2H structures represented by the formula MX_2 (M= Mo, W, and X = S, Se) as test-bed examples for highlighting the importance of symmetry in the determination of LF modes. Bulk MX_2 belongs to the point group D_{6h} and the primitive unit cell includes two M atoms and four X atoms (*i.e.*, each unit cell of the bulk includes two laterally shifted layers). It follows that there are 18 normal vibration modes at the Γ point of the Brillouin zone,[10,64,88] and the full representation is thus $\Gamma = A_{1g} + 2A_{2u} + 2B_{2g} + B_{1u} + E_{1g} + 2E_{1u} + 2E_{2g} + E_{2u}$, according to character tables. Among these modes, one of two (each doubly degenerated) E_{2g} modes corresponds to the Raman active shear mode (in-plane vibration), and one of the two B_{2g} corresponds to the optically inactive layer breathing mode (out-of-plane vibration). The other modes correspond to intralayer modes (Here we note the different concepts of intralayer and in-plane modes, as the former concept refers to the *origin* of the mode while the latter concept characterizes the *motion* of the atoms in the mode.) The shear mode has previously been referred to as the C mode: It was first observed in AB-stacked multilayer graphene (MLG),[57] and it provides a direct measurement of the interlayer *coupling*. Other notations of the shear modes, such as SM, and of layer-breathing modes as the B modes or LBM have been introduced by various research groups. For a general notation for interlayer vibration modes in

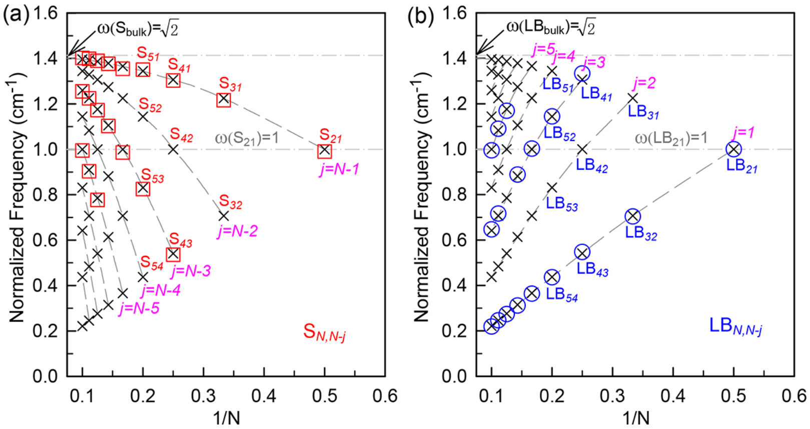

Figure 2. General results for the frequencies of S and LB modes *versus* the inverse of layer number *N* based on the LCM, where the frequencies of the S and LB modes in 2L ($\omega(S_{2,1})$ and $\omega(LB_{2,1})$) are normalized to 1. The squares in (a) and circles in (b) indicate the normalized experimental frequencies of the S and LB modes in multilayer MoS$_2$, respectively.[61] Reproduced with permission from ref 11. Copyright 2016 The Royal Society of Chemistry.

layered materials, here we denote the shear mode and the layer breathing mode as the S and LB modes, respectively. This should avoid any confusion as both S and LB modes are due to interlayer *coupling*. In MX$_2$, the frequencies of the S and LB modes are usually below 50 cm^{-1}. Historically, these modes have been collectively referred to as low-frequency (or LF) modes. Moving from the bulk to multilayer systems, the symmetry changes to D_{3d} and D_{3h} point groups for even and odd number of MX$_2$ layers, respectively.[10,64,89] Accordingly, the corresponding irreducible representations at the Γ point become: $\Gamma_{\text{even}} = \frac{3N}{2}(A_{1g} + A_{2u} + E_g + E_u)$, for N = 2, 4, 6, ..., and $\Gamma_{\text{odd}} = \frac{3N-1}{2}(A_1' + E'') + \frac{3N+1}{2}(A_2'' + E')$, for N = 1, 3, 5, ..., respectively. An NL MX$_2$ sample has $N - 1$ 2-fold degenerated S modes and $N - 1$ nondegenerated LB modes, as illustrated in Figure 1.[10,64] When N is even, the LB/S modes are either Raman-active (A_{1g}/E_g) or IR-active (A_{2u}/E_u). Conversely, when N is odd, the LB modes are either Raman-active (A_1') or IR-active (A_2''), while the S modes are either Raman-active (E'') or both Raman-active and IR-active (E').

The full identification of the S and LB modes requires the measurement of polarized Raman spectra.[10] Under a back-scattering configuration, the experimental polarization configuration is represented by the shorthand $\overline{Z}(XX)Z$ or $\overline{Z}(XY)Z$.[61,90,91] Here $\overline{Z}$ and Z are the propagation directions of incoming and scattering light, while XX and XY correspond to parallel and cross-polarization configurations, respectively. According to the Raman tensors for each phonon mode in MX$_2$, the LB modes can only be observed under the XX configuration, while the S modes can be observed under both XX and XY configurations.[61,64] This simple analysis shows a straightforward method to discern between the in-plane S modes and the out-of-plane LB modes by performing two distinct polarization Raman measurements.

Such analysis can be conducted for any 2DM, so long as its symmetry is clearly identified. The overall shape of the Raman tensor for a phonon mode (*i.e.*, the position of its nonzero elements) can be obtained by referring to space-group specific tabulated tensors. This establishes whether the mode is Raman active or not. Additionally, it also determines if the Raman mode can be observed or not under a specific polarization configuration. The actual intensity of the Raman active mode requires knowledge of the numerical values of the tensor elements. These can be obtained by computing the derivative of the polarizability tensor from first-principles.[92] In-depth discussions regarding the symmetry, Raman activity/tensor, and polarization dependence of phonon modes in diverse 2DMs can be found in previously published review articles.[10−12]

Linear Chain Model for Interlayer Modes. A fairly accurate picture of the physics of S and LB modes can be obtained using a simple LCM, where knowledge of atomistic details of the materials is not necessary but is replaced by a small number of parameters describing interlayer interactions. As shown in the rest of this review, this model works well in cases where the interactions between layers are weak compared to in-plane (*i.e.*, covalent or ionic) interactions. This condition is precisely met in layered materials where the interactions between layers are much weaker than the intralayer chemical bonding interactions, and thus each layer can be approximately treated as a rigid ball in the model.[93] Note that while this review will assume that the layers move rigidly or quasi-rigidly in the normal modes corresponding to low-frequency vibrations of interest, the rigidity is only approximate, especially for small-area flakes and for systems, such as TMDCs, where each layer is not strictly one-atom thick.[93] In fact, such approximation has proven to work very well for 2DMs. Based on this fact, we can model each layer as a single ball with mass density μ (μ is expressed in units of mass per unit area) to reveal the frequency ω of the S and LB modes in multilayer 2DMs. Usually, considering a multilayer sample with N layers, the nearest-neighboring layer force constant per unit area K is sufficient to yield accurate data in most cases. Note that exceptions exist, where next-nearest neighbors and beyond are necessary to provide a good agreement with experiment, as explained later.[83] As a general rule, for a N-layer in-plane isotropic material, there are $N - 1$ 2-fold degenerate S modes and $N - 1$ LB modes whose frequencies can be calculated by diagonalizing separate $N \times N$ dynamical matrices:[43,57,83]

$$\omega(S_{N,N-j}) = \omega(S_{\text{bulk}})\sin\left(\frac{j\pi}{2N}\right)$$

$$\omega(LB_{N,N-j}) = \omega(LB_{\text{bulk}})\sin\left(\frac{j\pi}{2N}\right) \qquad (1)$$

where the phonon branch index $j = 1, 2, 3, ..., N - 1$, $\omega(S_{\text{bulk}}) = (1/\pi c)\sqrt{K^{\parallel}/\mu}$, $\omega(LB_{\text{bulk}}) = (1/\pi c)\sqrt{K^{\perp}/\mu}$, $K^{\parallel}$ ($K^{\perp}$) is the in-plane (out-of-plane) nearest-neighboring interlayer force constant per unit area, μ is the total mass per unit area of each layer, and c is the speed of light in the unit of cm/s so that the frequency ω is expressed in cm^{-1}.[57] Note that a $\omega = 0$ 3-fold degenerated eigenvalue is found after matrix diagonalization. This mode belongs to the phonon (acoustic) branch $j = 0$ corresponding to a rigid translation of the entire material along the x, y, or z directions. Here for S/LB modes, we define $S_{N,1}/LB_{N,1}$ as the highest-frequency branch ($j = N - 1$) and $S_{N,N-1}/LB_{N,N-1}$ as the lowest-frequency branch ($j = 1$).[11,43,83] Note that a number of different notations have been used in the literature for different branches of S and LB modes in the publications from different groups.[19,64−66,80,94] According to eq 1, for a bilayer ($N = 2$, $j = 1$):

$$\begin{aligned} \omega(S_{2,1}) &= \omega(S_{\text{bulk}})/\sqrt{2} \\ \omega(LB_{2,1}) &= \omega(LB_{\text{bulk}})/\sqrt{2}, \end{aligned} \tag{2}$$

which shows that the interlayer mode frequency of the bulk is $\sqrt{2}$ larger than that in the bilayer case. When the frequencies of the S and LB modes in the bilayer are normalized to 1, the frequencies of the bulk are equal to $\sqrt{2}$, as shown in Figure 2.[11] As a general rule from the LCM, there exist two types of phonon branches for the S modes: (1) $j = N - 1, N - 2, N - 3, ...$, corresponding to the modes of $S_{N,1}$, $S_{N,2}$, $S_{N,3}$, ..., respectively, whose frequencies increase with increasing N; and (2) $j = 1, 2, 3, ...$, corresponding to the modes of $S_{N,N-1}$, $S_{N,N-2}$, $S_{N,N-3}$, ..., respectively, whose frequencies decrease with increasing N. This rule can also apply to the LB modes. Note that for a given N, the $N - 1$ doubly degenerate shear modes can also be simply denoted as S_1, S_2, S_3, ..., S_{N-1}, where the modes are ordered in such a way that the frequency monotonically decreases with increasing mode index. Similarly, the $N - 1$ LB modes can be denoted as LB_1, LB_2, LB_3, ..., LB_{N-1}. Figure 2 shows the branches of $j = N - 1, N - 2, N - 3, ...$ for the S modes and the branches of $j = 1, 2, 3, ...$ for the LB modes. In order to check the validity of such a general result, the normalized experimental frequencies of S and LB modes in $N \in 2-18$ for MoS_2[61] are also included as square symbols in Figure 2a and circles in Figure 2b, respectively. Clearly, the calculated values match very well with the experimental results. It is interesting to note that for naturally 2H-stacked MoS_2,[61] the observed S modes belong to the branches ($j = N - 1, N - 3, N - 5$) whose frequencies increase with increasing N, while the observed LB modes belong to the branches ($j = 1, 3, 5$) whose frequencies decrease with increasing N. The reason why these S and LB modes can be observed is revealed by a recently proposed interlayer bond polarizability model,[81,94] as discussed below in the section devoted to the interlayer bond polarizability model. The LCM within the approximation of nearest-neighboring interlayer coupling has been successfully applied to interlayer phonon frequency predictions for many 2DMs, such as graphene,[43,57,74,83] WSe_2,[64,95] $MoTe_2$,[96,97] Bi_2Se_3,[69] black phosphorus,[19,65,66] and ReS_2[68,79,80,98] and MoWS alloy.[99] In a few cases such as twisted two-dimensional samples, the LCM needs to include the second-nearest-neighboring interactions to yield quantitative agreement with experiment.[83]

In addition to predicting frequencies, the LCM also yields the eigen-displacements—or normal modes—of each LF mode. Specifically, for the j-th mode $S_{N,N-j}$ or $LB_{N,N-j}$ in a N-layer system, the displacement of layer i is[57]

$$\Delta r_i^j \propto \cos\left[\frac{j(2i - 1)\pi}{2N}\right] \tag{3}$$

where Δr_i^j is oriented along the x (or y) direction for S modes and along the z direction for LB modes. The vibrational patterns illustrated in Figure 1 can be reproduced by this equation.

Recent Advances in Low-Frequency Raman Scattering Techniques. The frequencies of the interlayer modes are usually well below 100 cm^{-1} and are therefore found to be close to the lower detection limit of typical Raman spectroscopes, which use a single monochromator integrated with a notch or edge filter. Since Raman spectroscopy measures the relative frequency shift between incident laser line and scattered Raman signal, LF Raman spectroscopy requires the excitation source to be a single-frequency laser with a very narrow line width. Generally, a single-frequency laser combined with a narrow line width bandpass filter is required for LF Raman measurements. Besides the laser source, the LF Raman measurements also require the equipment to efficiently suppress the strong Rayleigh line corresponding to elastic scattering. To achieve this, a subtractive mode is used in a triple monochromator Raman spectrometer, in which the first two monochromators serve as a tunable Raman filter and the third grating disperses the scattering light onto the detectors. Although the LF Raman signals are easily accessible by such a triple monochromator Raman spectrometer,[64,69,91] the throughput of this setup is really low, around 5 times lower than a single monochromator, leading to long acquisition time and to important limitations for its potential applications of weak signal detection.

Recently, major advances in notch filter fabrication based on the development of the volume Bragg grating (VBG) technique[100] have enabled the detection of LF Raman modes even in spectrometers using a single monochromator Raman system.[57,61] Each VBG-based notch filter (BNF) exhibits a narrow bandwidth (~8−10 cm^{-1}), high transmittance (up to 80−90% dependent on the laser wavelength), and an optical density (OD) 3−4. This makes it possible to measure LF Raman signals with high signal-to-noise ratio by a set of BNFs.[57,61] In order to effectively reject the Rayleigh line, 3−4 pieces of BNFs are usually used. The configuration of the three BNFs to a single monochromator is shown in Figure 3a. Bandpass filters (BPFs) based on the VBG technique are necessary to remove the plasma lines of the laser, whose spectral width can be as small as ~8−10 cm^{-1}. Since the BPF is a reflecting filter, at least two mirrors are necessary to precisely align the laser beam to the center of the first BNF (BNF1), as shown in Figure 3a. Three BNFs are usually well tuned to reach deep blocking of the Rayleigh line up to 10^{-9}−10^{-12}. After the filtering stage, LF Raman signals are effectively guided into the monochromator for detection. A major advantage of this technique is that the throughput of such Raman setup is much higher than the triple monochromator Raman spectrometer. Since the observation of the S mode in AB-stacked MLG using such a configuration and setup in 2012,[57] it has become increasingly popular to study LF interlayer modes in 2DMs[65,66,68,74,79,80,83,95−99] as well as the acoustic phonons in nanostructures.[101,102] Recently, thanks to further improvements of the VBG technique, the bandwidth of each BNF can be developed down to ~4 cm^{-1} at certain laser wavelength, and

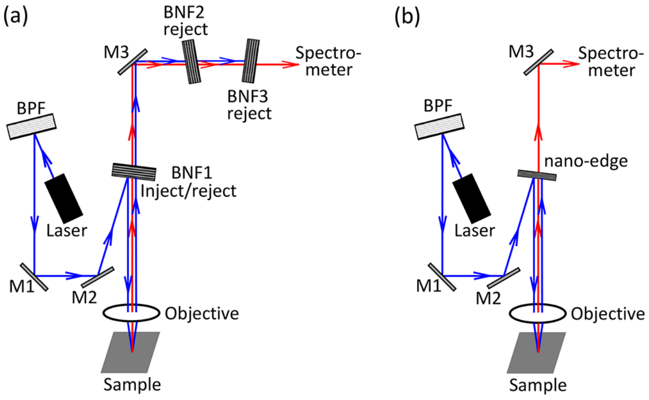

Figure 3. Schematic diagram of single monochromator LF Raman systems with (a) three VBG-based notch filters and (b) ultrasteep edge filter. M1, M2, and M3 are the mirrors to align optical paths. BNF1, BNF2, and BNF3 are three VBG-based notch filters. BPF is the VBG-based bandpass filter. Adapted with permission from refs 103 and 104. Copyright 2016 and 2017 American Institute of Physics.

thus the LF Raman measurements can be detected down to 2 cm^{-1}, approaching the Brillouin scattering regions.[103] This has been applied to reliably probe acoustic phonons in bulk semiconductors with high sensitivity, shortening the integration time of the Brillouin signal with a good signal-to-noise ratio by more than 2000-fold compared to a Fabry–Perot interferometer.[103]

In addition to VBG-based notch filters, specifically designed edge filters have been developed to probe LF Raman signal down to 10 cm^{-1}.[104] Such detection limit is often sufficient as most LF Raman modes of interest are mainly (but not exclusively) located above 10 cm^{-1}. The configuration of the edge filter to a single monochromator is shown in Figure 3b along with a VBG-based BPF to remove the plasma lines of the laser close to the Rayleigh line. A cross-polarized backscattering geometry can be used to suppress the Rayleigh line and obtain the LF Raman signal. This setup exhibits high sensitivity and easy operation, relying on commercial components, and makes it possible to obtain good LF Raman intensity with low excitation power and short acquisition time, as verified by the measurement to Ge/Si quantum dot superlattices and L-cystine.[104]

LOW-FREQUENCY RAMAN MODES FOR SAMPLE THICKNESS DETERMINATION

A number of experimental techniques have been devised to accurately identify the number of layers in 2DMs, including atomic force microscopy (AFM), photoluminescence (PL) techniques,[37,38,53,105−108] optical contrast measurement,[109−111] and HF Raman mode analysis.[53,54,74,112−114] However, the use of AFM may damage the sample and is not possible for suspended samples. Moreover, owing to the different interactions between the substrate and the sample, AFM measurements may lead to an inaccurate thickness determination.[53,96,115] Generally, PL only works for a limited number of 2DMs that possess a layer-dependent electronic bandgap. Thus, for semimetals, insulators or samples with poor PL signal, it is impossible to identify the number of layers based on PL measurements. Although the use of optical contrast techniques is straightforward and fast, it is strongly dependent on the substrate used.[53,109,111] It follows that the optical contrast is not the most reliable method to accurately determine the number of layers in a given sample. Measuring the frequencies of HF Raman modes can lead to useful information on the number of layers in some 2DMs,[10,54,74,112−114] but in most cases, this approach is only applicable to thin samples with $N < 5$. In stark contrast to all of these techniques, LF interlayer Raman scattering is exquisitely sensitive to interlayer coupling and to the number of layers. It has been successfully demonstrated as a convenient, fast, substrate-free, and reliable technique to

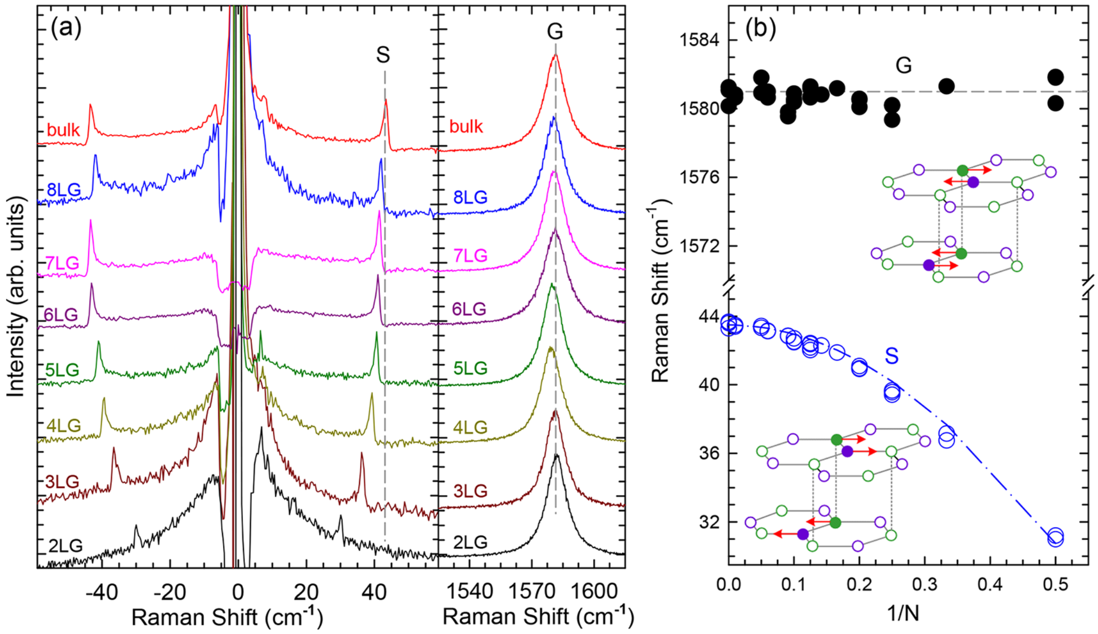

Figure 4. (a) LF and HF Raman spectra of 2−8L graphene and bulk graphite. The S peaks belong to $S_{N,1}$, the highest-frequency branch of S modes. (b) Experimental frequencies of G (filled black circles) and S (open blue circles) modes as a function of inverse layer number. The dashed line is based on the LCM. Adapted with permission from ref 57. Copyright 2012 Nature Publishing Group.

identify the number of layers, their stacking, and even the relative twisting angles between adjacent layers.

Multilayer Graphene. Graphene is the first truly 2DM that could be experimentally isolated into its mono- to few-layer configurations.[1] Usually, the number of graphene layers is experimentally determined by AFM, optical contrast,[109,110] or a measurement of the Raman line shape of the 2D Raman modes.[74,112,113] However, these methods present a number of limitations, as already mentioned above. In contrast, the measurement of the S modes in AB-stacked MLGs by LF Raman techniques offers an alternative approach to identify the number of graphene layers.[57] Figure 4a illustrates the observation of the highest-frequency branch of the S modes (*i.e.*, $S_{N,1}$) in 2−8L graphene and bulk graphite. In addition, Figure 4b shows the frequencies of the G and S modes as a function of $1/N$. The frequency of the $S_{N,1}$ mode is found to substantially increase as N increases, in agreement with expectations derived from the LCM presented in the section devoted to the LCM for interlayer modes. Note that the frequency of the G mode, observed at ∼1581 cm^{-1}, remains essentially constant as the number of layers increases. This suggests that the LF interlayer modes are more effective for thickness determination than the other techniques.

The LCM directly links the interlayer mode frequency with the interlayer coupling strength.[43,57,83] In MLGs, the interlayer shear coupling strength K has a value $\sim 1.28 \times 10^{19}$ Nm^{-3} as derived from the LCM.[57] This leads to an estimation of the interlayer shear modulus C_{44} of ∼4.3 GPa, which is consistent with the values between 4.5 and 5.1 GPa measured by inelastic X-ray scattering.[116] Similarly, the LB modes can also be used to identify the number of layers and interlayer coupling in AB-stacked MLGs. However, up to now, only a few works have reported the observation of the LB modes, using nonstandard conditions. For example, the second-order LB modes in MLGs have been observed by double resonance Raman scattering,[58,59] while first-order LB modes have been observed at high temperature.[60] Note that in contrast to the weak S and LB modes observed in AB-stacked MLGs, the S and LB modes in twisted MLGs (*t*MLGs) are significantly enhanced owing to the presence of strong resonance with additional optically allowed electronic transitions.[43,83]

We note that the S and LB modes in bulk graphite were investigated decades ago by inelastic neutron scattering.[117,118] The LB mode in bulk graphite is Raman inactive, and its frequency was determined around 128 cm^{-1} by neutron spectrometry (see Table 1).[83,117,118] The S mode in bulk graphite is Raman active, and thus its frequency can be obtained by both LF Raman scattering and inelastic neutron scattering (about 43.5 cm^{-1}).[57,117] The interlayer modes in bulk graphite give rise to two continuous branches of phonons for wave vector along the *c* axis (*i.e.*, the [001] direction), called TA (shear vibrations, doubly degenerated) and LA (breathing vibrations). At the A point of the first Brillouin zone, these branches are folded back in the direction of the Γ point due to the ABAB superstructure and become the TO and LO branches (note that different notations were used in other works).[117,118] At the Γ point, they correspond to the S and LB modes discussed in this work. Similar phonon dispersion analysis was also carried out previously for bulk MoS_2 by inelastic neutron scattering,[119] for bulk h-BN by inelastic X-ray scattering,[120] and for bulk black phosphorus by inelastic neutron scattering.[121,122] However, one should note that for bulk black phosphorus, the TA branch is split into two due to the in-plane anisotropy (*i.e.*, the two S modes are no longer degenerated).

Table 1. Summary of the Frequencies of the Bulk S and LB Modes ($\omega(S_{\mathrm{bulk}})$ and $\omega(LB_{\mathrm{bulk}})$) and the Corresponding in-Plane and out-of-Plane Interlayer Force Constants Per Unit Area ($K^{\parallel}$ and $K^{\perp}$)[a]

LMs	$\omega(S_{\mathrm{bulk}})$ (cm^{-1})	$\omega(LB_{\mathrm{bulk}})$ (cm^{-1})	$K^{\parallel}$ (10^{19} N/m^3)	$K^{\perp}$ (10^{19} N/m^3)
graphite	43.5	128[b]	1.28	11.1
MoS_2	32.5	56.8[c]	2.82	8.90
$MoSe_2$	25.5	48.1[d]	2.60	9.25
$MoTe_2$	26.8	39.3[e]	4.25	9.12
WS_2	27.5	47.8[f]	3.16	9.55
WSe_2	23.8	40.3[g]	3.06	8.77
$NbSe_2$	28.4	47[h]	2.92	8.00
h-BN	52.2	121[i]	1.83	9.83
Bi_2Te_3	25.4[j]	42.4[j]	4.57	13.33
Bi_2Se_3	18.0[j]	29.3[j]	2.27	5.26
PtS_2	40[k]	38[l]	6.27	5.11
$PtSe_2$	−	32[m]	−	5.09
ReS_2 (IS-stacked)	21.4[n]	41.4[n]	1.89	6.76
ReS_2 (AI-stacked)	24.7/19.5[n]	40.6[n]	2.54/1.55	6.76
black phosphorus	19.4/51.6[o]	87.1[o]	0.61/3.3[p]	12.7[q]

[a] For many bulk layered materials (LMs), the LB modes are either Raman inactive or cannot be observed under the common backscattering set-up. This is also true for the S modes in a few bulk LMs. In such cases, the values reported in the table are from other methods, such as inelastic neutron scattering, inelastic x-ray scattering, fitting with the LCM model using Raman data in few-layer systems or first-principles calculations. Part of the data are adapted with permission from ref 11. Copyright 2016 The Royal Society of Chemistry. [b] Neutron scattering data from refs 117 and 118. [c] LCM model fitting from ref 61 and also neutron scattering data from ref 119. [d] LCM model fitting based on eq 2 using the frequency of the bilayer Raman active LB mode from ref 52. [e] LCM model fitting from refs 96 and 97. [f] LCM model fitting from ref 132. [g] LCM model fitting from ref 64. [h] LCM model fitting from ref 71. [i] X-ray scattering data from ref 120. [j] LCM model fitting from ref 69. [k] DFT calculations from ref 138. [l] LCM model fitting from ref 138. [m] LCM model fitting from ref 139. [n] LCM model fitting from ref 79. [o] Neutron scattering data from refs 121 and 122. [p] DFT calculations from ref 137. [q] Experimental data from ref 66. Note that for ReS_2 in in-plane anisotropic (AS) stacking and black phosphorus, the frequencies of two S modes (S^x and S^y) are no longer equal, unlike other isotropic LMs.

Group 6 TMDCs MX_2. TMDC cystals, represented by the MX_2 (M = Mo, W; X = S, Se, Te) formula, have received extensive attention due to their distinctive electronic and optical properties. MX_2 multilayer samples feature a layered structure similar to MLGs. The frequencies of the S and LB modes of multilayer MX_2 can also be used to identify the number of layers and to shed light onto the interlayer coupling strength.[10,61,62,64] Figure 5a illustrates the LF Raman spectra of multilayer and bulk 2H-MoS_2, where a series of the S and LB modes are clearly observed below 50 cm^{-1}. As mentioned in the section devoted to the LCM, the observed S modes originate from the branches ($j = N - 1, N - 3, N - 5$) whose frequencies increase with increasing N, while the observed LB modes belong to the branches (j = 1, 3, 5) whose frequencies decrease with increasing N. For any thickness, the highest-frequency S mode, $S_{N,1}$, dominates the S peaks, while the lowest-frequency LB mode, $LB_{N,N-1}$, dominates the LB peaks.

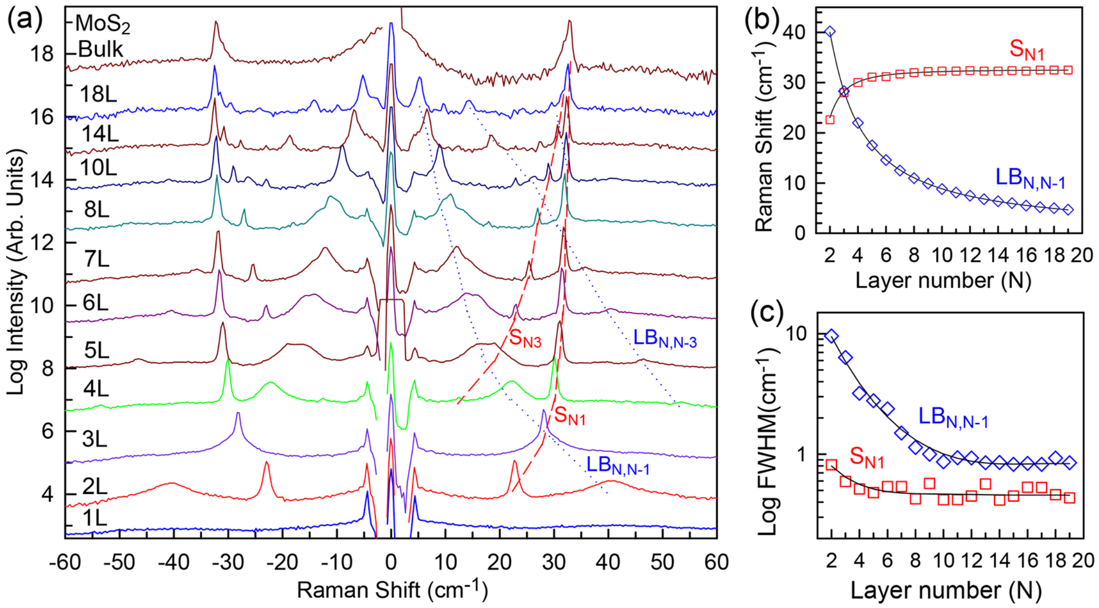

Figure 5. **(a) LF Raman spectra of 1−8L, 10L, 14L, 18L, and bulk 2H-MoS$_2$. (b) Frequency and (c) fwhm of the S and LB modes as a function of *N*. Reproduced with permission from refs 61 and 10. Copyright 2013 American Physical Society and copyright 2015 The Royal Society of Chemistry.**

Figure 5b−c shows their frequencies and full-widths at half-maximum (fwhm) as a function of *N*. In contrast to the small frequency variation (~3 cm^{-1}) of the HF E^1_{2g} and A_{1g} modes from bilayer to bulk,[54] the corresponding frequency variation of the S and LB modes is significant: ~$(\sqrt{2}-1)\omega(S_{2,1})$ (*i.e.*, ~10 cm^{-1}) for the S modes and ~$\omega(LB_{2,1})$ (*i.e.*, ~40 cm^{-1}) for the LB modes. Such contrast highlights the superiority of using LF modes for thickness determination. Note that the larger fwhm of the LB modes compared with the S modes can be explained by the anharmonic behavior related to the significant enhancement of phonon−phonon scattering.[10,63]

The frequency evolution of the LF modes with *N* in MX$_2$, for example, MoS$_2$, can be understood well within the LCM framework,[11,61] as shown in Figure 2. The LCM of MX$_2$ treats one M atom layer and two adjacent X layers as one ball, so such LCM is also denoted as the monatomic LCM or MCM. In order to elucidate whether the interaction of X−M atoms within an MX$_2$ layer affects interlayer coupling or not, Zhang *et al.* also included the force constant between the nearest M and X atoms within an MX$_2$ layer and regarded each M atom layer and each X atom layer as individual balls, which corresponds to a *diatomic* LCM (DCM).[61] The DCM of MoS$_2$ reveals that the relative displacement between Mo and S atoms within an MoS$_2$ layer can be ignored for all of the S and LB modes in *N*L-MoS$_2$. As a result, the calculated frequencies of the S and LB modes in *N*L-MoS$_2$ based on the DCM are identical to those obtained by MCM.[61] Similar to the graphene case, the shear modulus can be estimated on the basis of the interlayer force constant of *N*L-MoS$_2$,[10] with a numerical value of 18.9 GPa in agreement with reported value of 18.6 GPa based on phonon dispersion curves determined by neutron scattering and X-ray measurements of the linear compressibility properties.[61,123] Note that similar analyses have been conducted for other MX$_2$ materials as well.[10]

Davydov Splitting. In general, each phonon mode in a 1L system will split into *N* corresponding modes in *N*L. For example, each optical mode in 1L gives rise to a set of *N* near-degenerate vibrational modes in the corresponding *N*L system. Likewise, the acoustic modes in 1L will evolve into the S and LB modes in *N*L. The resulting modes are known as the Davydov components. Likewise, the frequency difference between two components is known as Davydov splitting. Such splitting is usually small because it results from a small perturbation to the strong intralayer vibration modes by the weak interlayer interaction and can be evaluated using a first-order approximation. Quantifying the Davydov splitting in *N*L TMDCs has proven to be a difficult task.[97,124−130] Song *et al.* have proposed a vdW model to quantitatively estimate the Davydov splitting of the A_1' or A^2_{1g} modes (denoted as A_1'-like modes for simplicity)[96] in *N*L MoTe$_2$. This approach was also extended to other Raman modes in *N*L TMDCs.[131] Taking the A_1'-like mode in *N*L MoTe$_2$ as an example, if the displacements between all the Te atoms of two adjacent layers are in-phase, the frequency of the corresponding A_1'-like mode in the *N*L MoTe$_2$ is equal to that (ω_0) of the A_1' mode in 1L MoTe$_2$. In contrast, if one or more pairs of out-of-phase displacements between two adjacent Te atom layers exist in the j^{th} A_1'-like mode in *N*L MoTe$_2$ (j = 1, 2, 3,..., $N-1$), its frequency (ω_j) will slightly depart from ω_0 due to the interlayer coupling from the out-of-phase displacements between two adjacent Te atom layers. Within the first-order approximation, the frequency of the corresponding LB mode with similar out-of-phase displacements between two adjacent Te atom layers can be considered as the perturbation from ω_0, *i.e.*, the coupling frequency ($\Delta\omega_j$). In this case, the frequencies of the A_1'-like mode in *N*L MoTe$_2$ and the A_1' mode in 1L MoTe$_2$ can be directly linked by $\omega_j^2 = \omega_0^2 + (\Delta\omega_j)^2$, where the coupling frequency $\Delta\omega_j$ is the frequency of the corresponding LB mode. Note that due to the direction of the displacements, for the in-plane E'-like modes in *N*L MoTe$_2$, the coupling frequency is the frequency of the corresponding S mode.

The observation of Davydov components is related to the electron−phonon coupling and Raman activity. Only about half of the Davydov components can be Raman active in multilayer TMDCs. For example, the A_1' mode in 1L MoTe$_2$ leads to the emergence of $(N+1)/2$ and $N/2$ Raman active modes in odd-

DOI: 10.1021/acsnano.7b06551
ACS Nano 2017, 11, 11777−11802

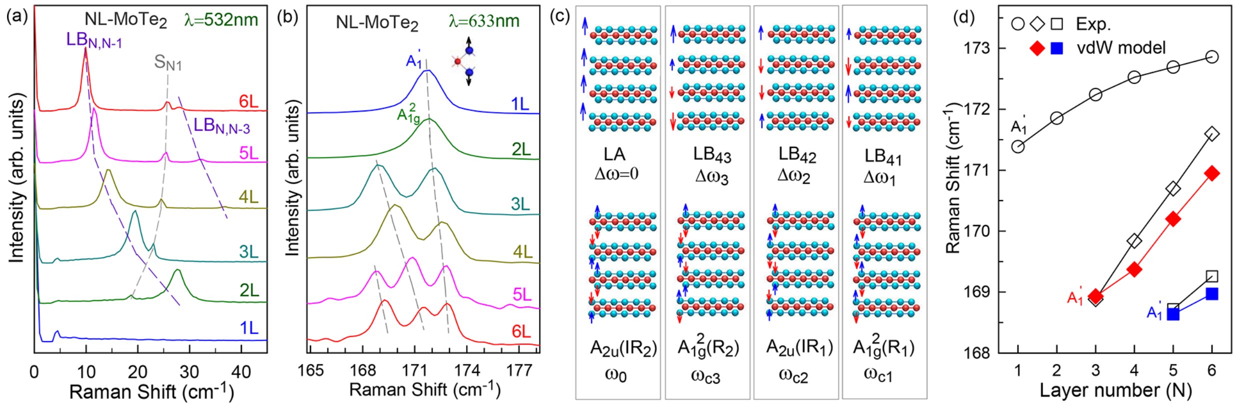

Figure 6. (a) LF and (b) HF Raman spectra of 1−6L $MoTe_2$. For any thickness in (a), $S_{N,1}$ is the highest-frequency branch of S modes, while $LB_{N,N-1}$ and $LB_{N,N-3}$ are the lowest- and third lowest-frequency branches of LB modes, respectively. (c) Schematic of atomic displacements of LB and A_1'-like modes in 4L $MoTe_2$. (d) Calculated values (solid symbols) from vdW model and experimental A_1'-like modes (hollow symbols) in 1−6L $MoTe_2$. Adapted with permission from refs 96 and 53. Copyright 2016 American Physical Society and copyright 2017 John Wiley & Sons, Inc.

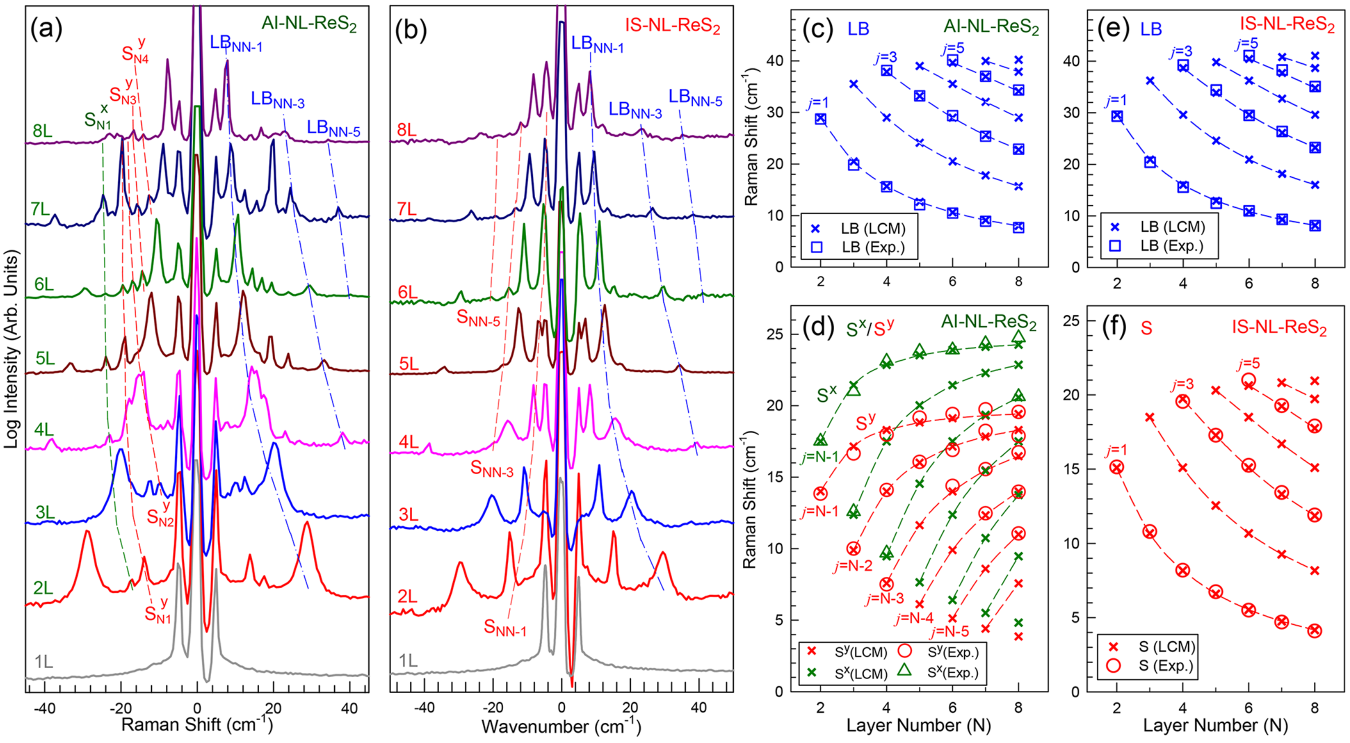

Figure 7. LF Raman spectra of (a) AI-stacked and (b) IS-stacked ReS_2. (c−f) Experimental frequencies of LB and S modes as a function of N for ReS_2 in AI and IS stacking orders. Corresponding calculated values based on the LCM are also shown for comparison. Reproduced with permission from ref 79. Copyright 2016 Royal Society of Chemistry.

and even-layer $MoTe_2$, respectively, among the total N Davydov components.[53,96] Therefore, the Davydov splitting cannot be observed in 2L $MoTe_2$. Under resonant conditions, only two Davydov components can be observed in 3L and 4L $MoTe_2$. Figure 6 depicts the LB and A_1'-like modes in 1−6L $MoTe_2$, the atomic displacements of the LB and A_1'-like modes of 4L $MoTe_2$, and the corresponding experimental and vdW model data.[96] The figure shows that the vdW model can be used to explain the Davydov splitting of the A_1'-like mode in NL $MoTe_2$.[96] Such Davydov splitting is N-dependent, and thus the corresponding spectral features can also be used for sample thickness determination. It has also been reported that under resonance conditions at low temperature, the forbidden Davydov components in WS_2 can also be observed by Raman scattering.[130]

Helicity-Resolved Raman. Thanks to their different normal mode symmetries, the S and LB modes can be distinguished by linearly polarized Raman scattering measurements.[61,64] They can also be identified by helicity-resolved Raman scattering by controlling the helicity of the incoming and outgoing photons. This type of measurement has been demonstrated by Chen *et al.*, who measured helicity-resolved LF Raman modes in MoS_2, WS_2, $MoSe_2$, and WSe_2.[132] The switching of the photon angular momentum by zone-center optical phonons depends sensitively on the different symmetry properties of the phonon modes. While the LB mode preserves photon helicity, the S mode

DOI: 10.1021/acsnano.7b06551
ACS Nano 2017, 11, 11777−11802

reverses photon helicity. In other words, the LB and S modes can be measured in $\overline{Z}(\sigma^+\sigma^+)Z$ and $\overline{Z}(\sigma^+\sigma^-)Z$ polarization configurations, respectively.[132] This shows that helicity-resolved Raman spectroscopy may be another powerful approach for characterizing LF Raman modes and interlayer coupling in 2DMs.

In-Plane Anisotropic ReX$_2$. Unlike isotropic MoS$_2$, ReX$_2$ (X = S, Se) crystals exhibit a distorted CdCl$_2$-type lattice structure with in-plane anisotropy. In-plane lattice distortion profoundly affects the interlayer coupling in such multilayer samples.[67,68,79,80,98] In contrast to isotropic materials like MoS$_2$, the electronic bandgap of ReS$_2$ remains direct regardless of the number of layers,[6] similar to in-plane anisotropic black phosphorus, for instance.[18,38,107,108] Owing to the in-plane anisotropy, the two S modes are no longer degenerate in ReS$_2$, and, more generally, the LF Raman modes are different compared to MoS$_2$ and graphene. In particular, multilayer ReS$_2$ samples obtained by mechanical exfoliation from natural bulk materials show a variety of stacking orders,[79] which makes it more difficult to develop a full understanding of the LF Raman spectra of multilayer ReS$_2$, compared to isotropic systems. Figure 7a−b illustrates this complexity by showing the LF Raman spectra of N-ReS$_2$ (N = 1−8) with two types of stacking orders: in-plane anisotropic (AS) and isotropic (IS) stacking configurations, respectively.[79] It shows that, for the same number of layers, the S modes in ReS$_2$ display different behaviors between the AS and IS stacking orders, while the LB modes are almost identical between the two stacking configurations.[79] As a result, in spite of the existence of in-plane anisotropy and different stacking orders in multilayer ReS$_2$, the frequencies of LB modes can still be used to identify the number of layers in the sample.

According to eqs 1 and 2, the frequency of the j-th LB mode in N-layer ReS$_2$ is $\omega(\mathrm{LB}_{N,N-j}) = \sqrt{2}\,\omega(\mathrm{LB}_{2,1})\sin\left(\frac{j\pi}{2N}\right)$, where $\omega(\mathrm{LB}_{2,1})$ is the frequency of the LB mode in bilayer ReS$_2$. This relation can also be applied to the S modes. It should be noted that, in the AS configuration, the description of each S mode branch splits into two distinct equations:

$$\omega(\mathrm{S}^x_{N,N-j}) = \sqrt{2}\,\omega(\mathrm{S}^x_{2,1})\sin\left(\frac{j\pi}{2N}\right)$$

and

$$\omega(\mathrm{S}^y_{N,N-j}) = \sqrt{2}\,\omega(\mathrm{S}^y_{2,1})\sin\left(\frac{j\pi}{2N}\right)$$

The experimental results of AI and IS configurations and calculated values are summarized in Figure 7c−f,[79] where j = 1, 3, 5 branches of the S and LB modes have been observed in IS-stacked NL ReS$_2$. However, the $j = N - 1$ branch of the S^x modes, $j = N - 1$, $N - 2$, $N - 3$, $N - 4$ branches of the S^y modes and j = 1, 3, 5 branches of the LB modes have been observed in AI-stacked NL ReS$_2$. Such difference between IS- and AI-stacked NL ReS$_2$ demonstrates different lattice dynamics and symmetries between the two stacking configurations and would require further investigation to develop a full understanding.

Because the S and LB modes in ReS$_2$ can also be well understood by the LCM, the interlayer coupling strength is expected to be a constant in multilayer ReS$_2$ for a given stacking order. Based on the observed $\omega(\mathrm{LB}_{2,1})$ and $\omega(\mathrm{S}_{2,1})$ in 2L ReS$_2$, we find that the interlayer shear force constants $K^{\parallel}$ of AI-stacked ReS$_2$ along the x and y directions are around 90% and 55% of those of MoS$_2$,[79] while this ratio is around 67% for $K^{\parallel}$ in IS-stacked ReS$_2$. The interlayer breathing force constant $K^{\perp}$ in AI- and IS-stacked ReS$_2$ is around 76% of that in MoS$_2$.[79] These results suggest that the interlayer coupling in ReS$_2$ is relatively strong and plays an important role in the determination of its optical properties.[79]

Other Layered Materials. *NbSe$_2$.* NbSe$_2$ is another example of TMDCs featuring a layered structure. However, in contrast to most of the other TMDCs, NbSe$_2$ is a conductor which exhibits a number of properties usually found in strongly correlated materials, such as superconductivity at T_C = 7.2K[133] and charge density waves (CDW) at T_CDW = 33.5K.[134] The interlayer interaction is key to describing the evolution of T_CDW and to a lesser extend T_C as a function of the number of layers. Xi *et al.* observed that T_CDW continuously increases as the number of layers decreases to reach a value of 145 K for the monolayer.[70] In contrast, T_C is only mildly sensitive to the number of layers, as it monotonically reaches a value of 3.1K for monolayers.[135,136] While the interlayer phonons play a crucial role in increasing the CDW transition temperature, the transition itself does not affect the phonons as demonstrated by He *et al.*[71] As shown in Figure 8a, for NbSe$_2$, the highest-frequency S mode (S$_{N,1}$) and the lowest-frequency LB mode (LB$_{N,N-1}$) have the strongest Raman signals, with the frequencies of the S and LB modes increasing and decreasing as a function of the number of layers, respectively. The crossover between the S and LB mode occurs for three layers, where the two frequencies coincide at about 24 cm^{-1}. It is interesting to note that the LF Raman scattering (both S and LB modes) in NbSe$_2$[71] is similar to that in MoS$_2$[61,64] discussed above in the section devoted to group 6 TMDCs MX$_2$, although the details of their stacking are different. Natural NbSe$_2$ is in the 2Ha phase (or AB′ stacking), while natural MoS$_2$ is in the 2Hc phase (or AA′ stacking). Nevertheless, the interlayer bond polarizability model discussed below shows a general rule that 2DMs in AA′ stacking (like MoS$_2$, MoSe$_2$, MoTe$_2$, WS$_2$, WSe$_2$, and h-BN), AB′ stacking (like NbSe$_2$), and

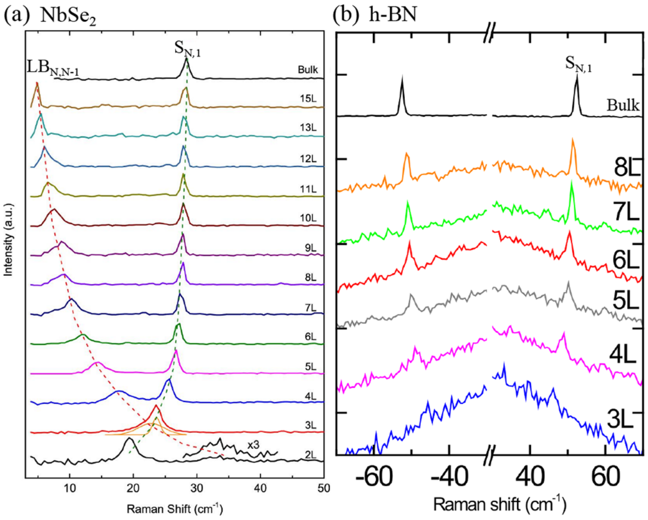

Figure 8. LF Raman spectra of (a) NbSe$_2$ and (b) h-BN as a function of number of layers. In (a), S$_{N,1}$ is the highest-frequency branch of S modes, while LB$_{N,N-1}$ is the lowest-frequency branch of LB modes. In (b), both Stokes/anti-Stokes data are shown, where S$_{N,1}$ peaks can be seen. Adapted with permission from refs 71 and 72. Copyright 2016 and 2017 Institute of Physics.

AB stacking (like graphene) exhibit similar LF Raman scattering.[81] Specifically, the highest-frequency S branch, $S_{N,1}$, dominates the S peaks, while the lowest-frequency LB branch, $LB_{N,N-1}$, dominates the LB peaks.

h-BN. Hexagonal boron nitride (h-BN), also called *white graphene*, is a two-dimensional insulator with a wide bandgap (~6 eV) featuring an atomic structure very similar to that of graphene. It attracts significant interest owing to its potential as a complementary component, such as an encapsulation layer or an ideal dielectric substrate, in the design of functional two-dimensional heterostructures.[72] The large bandgap corresponds to an energy well above most laser excitation energies used in Raman spectroscopy. It follows that Raman scattering in h-BN typically falls in the nonresonant condition, giving rise to weak Raman signals. As a result, the detection of the LF modes in multilayer h-BN is rather challenging, and it was only achieved recently by Stenger *et al.*[72] Similar to MLG (Figure 4), the highest-frequency branch of the S modes, $S_{N,1}$, dominates in the LF Raman scattering of h-BN samples, as shown in Figure 8b. Starting from 3L to bulk, the S-mode frequency increases from ~46.0 to 52.5 cm^{-1}. This result can also be validated by the LCM.[72] On the other hand, the characteristic HF mode at 1366 cm^{-1} shows little change in frequency as a function of the number of layers. This highlights the promise of LF Raman spectroscopy as a tool to quantitatively determine the thickness of h-BN samples.

Black Phosphorus. Black phosphorus (BP) is the most stable allotrope of phosphorus. It is characterized by a layered structure where each monolayer has a puckered and anisotropic structure.[14−16] Raman spectroscopy has been used extensively to characterize its structural properties, specifically the characteristic HF A_g^1, B_{2g}, and A_g^2 modes found in all BP samples, regardless of the number of layers. In the LF region, multiple LB peaks can be observed in BP under typical experimental backscattering configurations with frequencies strongly dependent on the number of layers.[19,65,66] For orthorhombic BP, the symmetry of the S modes requires a nonbackscattering configuration, such as $\overline{Z}(YZ)Z$ or similar, to be used to make them detectable by Raman measurements.[19,65] Among the observed LB modes, two prominent bands arise from the lowest-frequency branch (*i.e.*, $LB_{N,N-1}$) and highest-frequency branch (*i.e.*, $LB_{N,1}$).[65] The LCM theory can account for the fact that in contrast to the lowest-frequency mode $LB_{N,N-1}$ whose frequency decreases as a function of N, the highest-frequency mode $LB_{N,1}$ increases in frequency as a function of N.[65] Furthermore, Dong *et al.* reported observation of an unusual ultralow frequency mode, called the collective compression mode (CCM), that has an in-phase compression motion of all the layers in the BP sample relative to the substrate.[66] Its frequency quickly decreases with increasing N. This effect cannot be fully explained by the conventional LCM, and this mode was attributed to the strong interlayer coupling in BP. In fact, the derived interlayer out-of-plane force constant in BP is larger than that of graphene and MoS_2.[65,66] This is an important result indicating that the interaction between BP layers is not of pure dipole−dipole (*i.e.*, vdW) type but also involves significant electron density overlap stemming from the presence of P's lone electron pairs.[65,137]

PtS_2 and $PtSe_2$. PtS_2 and $PtSe_2$ are other examples of layered structures where stronger than vdW interlayer interaction governs the appearance of S and LB modes between quasi-rigid layers.[138,139] This strong interaction also stems from the hybridization of interlayer chalcogenide atoms, which yields a significant overlap of the electronic densities between layers and an appreciable degree of covalent (*i.e.*, directional) interlayer bonding.[137] This effect can be quantified using Raman measurements by fitting the force constants used in LCM's equations to show that the interlayer breathing force constant (IBFC) and interlayer shear force constant (ISFC) are almost identical in PtS_2, in contrast to other structures governed by vdW interlayer interaction (such as graphene or MoS_2 where IBFC > ISFC). In PtS_2 and $PtSe_2$, the LB modes can be observed in LF Raman spectra and the lowest-frequency LB branch is the most prominent peak. Its peak position quickly redshifts with increasing number of layers, thereby serving as an effective thickness indicator.[138,139]

Bi_2Te_3 and Bi_2Se_3. Bi_2Te_3 and Bi_2Se_3 are examples of 2DMs with topological insulator properties. Each individual layer features quintuple atomic layers, which are interlinked by covalent bonds. These individual layers hold together to form a multilayer by weak interlayer interactions. The absence of interlayer vibration modes in the Raman spectra of the bulk is a distinct feature of these topological insulators compared to bulk graphite and MoS_2, because the stacking in Bi_2Te_3 and Bi_2Se_3 assumes a unique ABC configuration.[69] This effect can be explained by the interlayer bond polarizability model discussed in details below.[81] The ABC stacking order also dictates that both the lowest-frequency S and LB branches lead to prominent LF Raman peaks, with frequencies quickly decreasing with increasing number of layers (see Figure 12g). Finally, before concluding this section, in Table 1 we summarize the frequencies of the bulk S and LB modes of the layered materials discussed in this review. With the bulk frequencies, the frequencies of all S and LB modes in an N-layer system can be obtained by the LCM theory (eq 1). In addition, they can also lead to an accurate estimation of the in-plane and out-of-plane interlayer force constants (Table 1).

LOW-FREQUENCY RAMAN MODES AS FINGERPRINTS OF STACKING CONFIGURATION

In addition to determining the number of layers, knowing the exact sequence of layers is of crucial importance to describe the properties of 2DMs. For example, starting with graphene, twisted bilayer graphene exhibits distinct electronic and optical properties compared to bilayers featuring the common Bernal (AB) stacking. These properties include fractional quantum Hall effect, presence of Van Hove singularities, *etc.*[39−42,140,141] Graphene trilayers with common ABA (Bernal) and ABC (rhombohedral) stacking orders exhibit considerably different electronic structures, infrared absorption spectra, electronic bandgap tunability, and quantum Hall effect.[44−47,86,142] For instance, the ability to open an electronic bandgap in graphene systems remains of great fundamental and practical interest in the quest of using graphene in nanoelectronics and optoelectronics. Graphene trilayers with the typical ABA stacking do not display any appreciable gap in the presence of an external electric field. Conversely, graphene trilayers with ABC stacking do feature the development of a large bandgap under the influence of an applied electric field, owing to the stacking-dependent electronic interactions and symmetries.[45−47]

Many other layered compounds that have been (re)-discovered in the context of 2DMs provide a seemingly unlimited playground for studying stacking-dependent phenomena.[47] For instance, group 6 TMDCs MX_2 (M = Mo, W; X = S, Se, Te) constitute another set of examples of 2DMs with

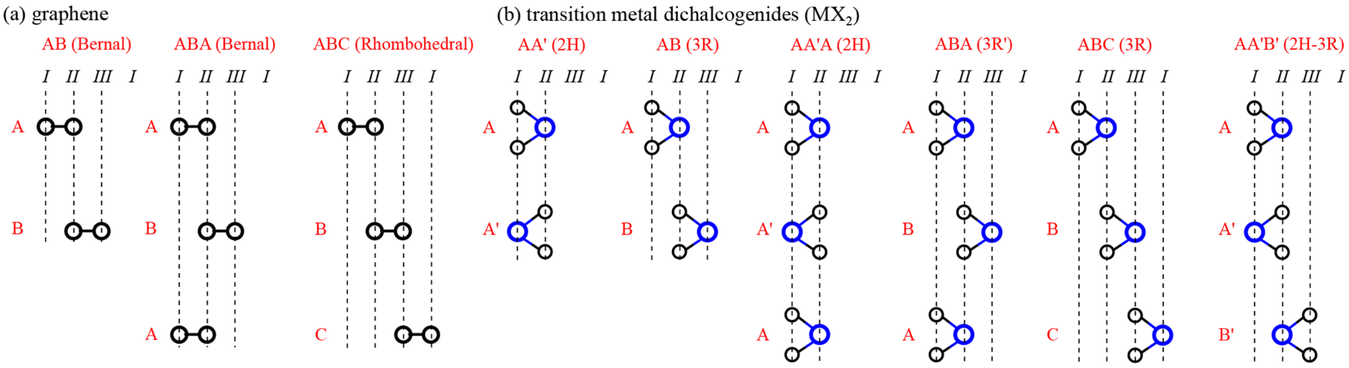

Figure 9. Schematic of common stacking sequences of bilayer and trilayer graphene and MX_2. In MX_2, the blue (black) circles represent metal M (chalcogenide X) atoms. In the honeycomb lattice, there are three atomic coordinates: *I*: 0, 0; *II*: 1/3, 2/3; *III*: 2/3, 1/3. Each letter in the stacking sequence stands for one layer. Adapted with permission from ref 81. Copyright 2017 The Royal Society of Chemistry.

tremendous research interest and technological promises. Among all known TMDCs, MoS_2 is the most studied.[4] Bulk MoS_2 exhibits two stable stacking polytypes, 2H and 3R, with different symmetries but with similar formation energies.[3,8,76] At the other end of the spectrum, monolayer MoS_2 exhibits strong spin−orbit coupling and a broken inversion symmetry. In addition, the spin and valley are inherently coupled, leading to valley-contrasting optical dichroism for valleytronics.[76,143,144] However, because bilayer MoS_2 in 2H stacking restores the inversion symmetry, the valley-contrasting optical selection rule becomes invalid.[42,48,76,145] In principle, for 2H-MoS_2, only odd-layer systems with no inversion symmetry can present spin/valley polarization, while even-layer and bulk systems cannot because of the presence of inversion symmetry.[48,76] In contrast, 3R-MoS_2 is noncentrosymmetric regardless of the thickness, and hence valley-contrasting optical dichroism is allowed regardless of the parity of N.[42,48,76] Interestingly, the piezoelectric effect is also sensitive to symmetry and can be forbidden when inversion symmetry is present. Recent pioneering works have demonstrated that piezoelectricity is present and absent in odd-layer and even-layer 2H-MoS_2, respectively, due to the breaking and recovery of the inversion symmetry.[146,147] However, since inversion symmetry is always broken in 3R-MoS_2, piezoelectricity could be present in the 3R stacking for any thickness. This is just an example of the level of tunability stacking order offers to tailor the properties of 2DMs.

Although atomic-resolution scanning transmission electron microscopy (STEM) is one of few techniques that can be used to determine the exact atomic registry between different layers,[52] LF Raman spectroscopy has recently risen as a fast and inexpensive optical technique for routine stacking characterization, and it could become an affordable tool in any laboratory. In this section, we first discuss the nomenclature of stacking in popular 2DMs and propose a general strategy to unify the stacking terminology in the field.[81] We then review the experimental progress on the stacking determination by LF Raman modes in 2DMs. The stacking dependence of LF Raman intensities can be understood by combining group theory, the generalized interlayer bond polarizability model, and first-principles-based simulations.

Unified Stacking Nomenclature. The most common stacking pattern in bilayer graphene is the AB or Bernal configuration (Figure 9a), which corresponds to every other carbon atom in one layer eclipsed over an atom in the other layer and the other atoms directly positioned over the center of a hexagon of the second layer. Compared to the less common and less stable AA stacking where the layers are exactly aligned, AB stacking has the second layer shifted over the length of one carbon bond with respect to the first layer. For this reason, this configuration is often referred to as the *staggered* stacking. In trilayer graphene, the first and second layers assume AB stacking, and, when adding a third layer, the shift can be undone, resulting in ABA (Bernal) stacking sequence, or repeated, to yield ABC (rhombohedral) stacking sequence (Figure 9a).[47]

For group 6 MX_2 like MoS_2, the presence of two distinct chemical elements in the unit cell gives rise to more diverse high-symmetry stacking configurations compared to graphene. As discussed above, bilayer MoS_2 has two stable stackings, which are similar to the bulk 2H and 3R stacking polytypes, respectively.[49,50,148,149] Likewise, trilayer MoS_2 has more complex stacking combinations beyond 2H and 3R.[52,149] Currently there is no universal stacking nomenclature to uniquely describe few-layer MoS_2. Different works have adopted a set of different terminologies, and this creates unnecessary confusion in the community.[51,52,75,76,94,148−150] This is the reason why the notations used for the bulk (*i.e.*, 2H and 3R) are still widely used for labeling stacking orders in multilayer systems, even though strictly speaking they are neither entirely valid nor sufficient to describe the types of stacking found in multilayer samples. For example, for bulk crystals in 2H and 3R, the letters stand for hexagonal and rhombohedral, respectively, and the digit indicates the number of layers in one unit cell.[8] It follows that using the label 3R in two-layer samples is not a strictly correct term. Of course, the use of 2H and 3R terminology is still useful as it serves as a common starting point. In this review, we adopt a well-accepted methodology to unify the stacking nomenclature in group 6 TMDCs, also applicable to other hexagonal structures including graphene, h-BN, GaS(Se), $NbSe_2$, *etc.*[81,85,148,150,151] The labeling is described as follows: For bilayer MX_2 shown in Figure 9b, 2H stacking corresponds to M in one layer over X in the other layer and X in one layer over M in the other layer (*eclipsed* with M over X), or AA′ in short; 3R stacking corresponds to M in one layer over X in the other layer, while all other M and X over the hexagon centers (*staggered* with M over X), known as AB. Note that 2H stacking cannot be named as AA since AA is reserved for an unstable stacking configuration, where M in one layer is over M in the other layer, and X in one layer is over X in the other layer.[81,84,85] Starting from AA′ and AB stackings in a bilayer system, four types of stacking combinations can be present in trilayer MX_2:

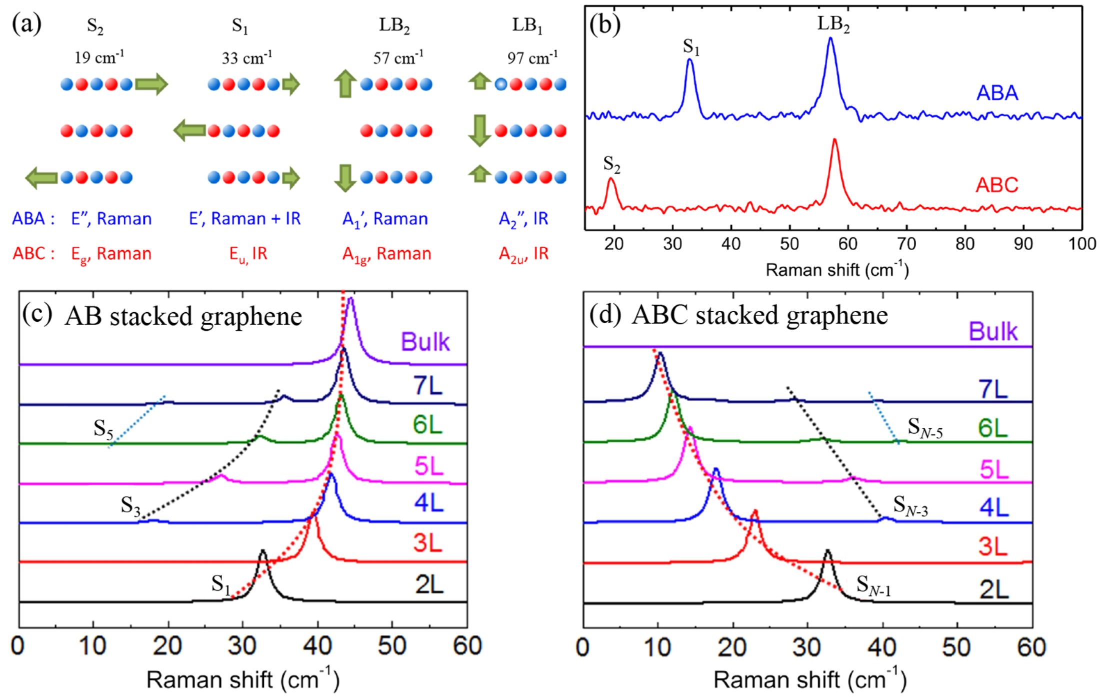

Figure 10. (a) Atomic displacements for LF modes of ABA- and ABC-stacked trilayer graphene. The arrows indicate both magnitude and direction of the layer−layer vibrations. (b) Experimental LF Raman spectra for suspended ABA (blue) and ABC (red) trilayer graphene. First-principles calculated LF Raman spectra for (c) AB and (d) ABC stacked MLG and bulk graphite. Dashed lines are guides for the eyes for the frequency evolution trend of the shear modes. (a and b) Adapted with permission from ref 73. Copyright 2015 American Institute of Physics. (c and d) Adapted with permission from ref 94. Copyright 2015 Nature Publishing Group.

AA′A, ABA, ABC, and AA′B′ (each letter in the stacking sequence corresponds to each individual layer, Figure 9b). It appears from this definition that the notation AA′A corresponds to 2H stacking in the trilayer system, while AA′B′ (A′B′ equivalent to AB) is a mixture of 2H and 3R stackings, also labeled 2H-3R. Likewise, ABC corresponds to the bulk 3R stacking, while ABA is another form of 3R stacking (labeled 3R′). In short, four types of high-symmetry stacking configurations can exist in trilayer MX_2, and two of them can be traced back to the bulk 2H and 3R stacking polytypes, while the other two are their combinations or derivatives. Each of these stacking orders have been experimentally studied in a number of recent reports.[52,75−78,94] Note that all four stacking types discussed can also be found in bulk GaSe samples, where AA′A, ABA, ABC, and AA′B′ are historically referred to as β-2H, ε-2H, γ-3R, and δ-4H polytypes, respectively.[152,153] In addition, although bulk $NbSe_2$ is also in the 2H phase, the stacking order assumes AB′ (*staggered* with Nb over Nb, while Se atoms over the hexagon centers),[71,81] different from AA′ stacking of 2H-phase MoS_2. This further demonstrates the usefulness of the stacking terminology for unambiguous stacking assignment.

Multilayer Graphene. Recent works have demonstrated the unique dependence of LF Raman intensities on the stacking configuration in few-layer graphene.[73,74,94] Lui *et al.* reported that in trilayer graphene of either ABA or ABC stacking, there are two double-degenerate shear modes (S_2 and S_1) and two layer breathing modes (LB_2 and LB_1), as shown in Figure 10.[73] Note that in this section, the notations $S_{N,j}$ and $LB_{N,j}$ will be simplified as S_j and LB_j, respectively. Since ABA- and ABC-stacked trilayers share very similar interlayer coupling, the frequencies and vibrational patterns of these LF modes show little variations upon stacking change. However, their symmetry assignments, Raman and infrared (IR) activity can be strongly stacking-dependent. ABA trilayers present a mirror symmetry with the point group D_{3h}, and consequently the S_2 and S_1 modes assume E″ and E′ symmetries, respectively (Figure 10a). Although both modes are Raman active, their Raman tensors are different according to group theory:[154]

$$\vec{R}(\mathrm{E''}) = \begin{pmatrix} 0 & 0 & c \\ 0 & 0 & d \\ c & d & 0 \end{pmatrix}, \quad \vec{R}(\mathrm{E'}) = \begin{pmatrix} a & b & 0 \\ b & -a & 0 \\ 0 & 0 & 0 \end{pmatrix} \tag{4}$$

Based on the Placzek approximation, the Raman intensity of a phonon mode is given by $I \propto |\vec{e}_{\mathrm{i}} \cdot \vec{R} \cdot \vec{e}_{\mathrm{s}}^{\,T}|^2$, where $\vec{R}$ is the second-rank Raman tensor of the phonon mode, and $\vec{e}_{\mathrm{i}}$ and $\vec{e}_{\mathrm{s}}$ are the electric polarization vectors of the incident and scattered light, respectively.[19,73,92,155,156] This equation explicitly shows that the Raman intensity depends on the Raman tensor and the scattering geometry, which are intrinsic and extrinsic properties, respectively. The most common scattering geometry is the backscattering one where the laser polarizations are parallel to the sample plane (x, y). According to eq 4, the Raman intensity of the S_2 mode with E″ symmetry is zero, whereas that of the S_1 mode with E′ is finite. This explains why S_2, though Raman active, is not observed in the Raman spectrum of ABA stacked samples (Figure 10b).

In contrast, ABC trilayers feature inversion symmetry with the point group D_{3d}, and consequently the S_2 and S_1 modes assume E_g and E_u symmetries, respectively (Figure 10a). Their Raman tensors are also different:

$$\vec{R}(\mathrm{E_g}) = \begin{pmatrix} e & f & 0 \\ f & -e & 0 \\ 0 & 0 & 0 \end{pmatrix}, \quad \vec{R}(\mathrm{E_u}) = \begin{pmatrix} 0 & 0 & 0 \\ 0 & 0 & 0 \\ 0 & 0 & 0 \end{pmatrix} \tag{5}$$

The S_1 mode with E_u symmetry has a zero Raman tensor and thus is Raman inactive, while the Raman intensity of the S_2 mode with E_g symmetry is finite in the in-plane polarization configuration. This explains why S_1 is not observed in Figure 10b for ABC stacking. As a result, the S_1 (S_2) mode is observed exclusively in the Raman scattering of ABA (ABC) stacking sequence, which is dictated by the stacking-sensitive crystal symmetry. On the other hand, Raman peaks of the high-frequency modes including D, G, and 2D modes exhibit less pronounced stacking dependence. Such a sensitive LF Raman response suggests that the shear modes can offer a promising alternative to characterize the stacking order for few-layer graphene.[73] Note that the LB modes do not share a similar sharp stacking dependence as that shown for the S modes. The LB_2 mode in either stacking order presents a similar form for Raman tensor and hence shows similar Raman intensities for ABA and ABC stackings, while the LB_1 mode is Raman inactive and cannot be observed in either stacking (Figure 10b).

Interlayer Bond Polarizability Model. So far, this review has largely focused on showing how symmetry analysis based on the premises of group theory can provide a qualitative understanding of LF Raman modes. We will now show that a quantitative description can be obtained using the interlayer bond polarizability model developed by Liang *et al.*[81] and indicate how the model can also offer an intuitive explanation of the stacking-sensitive LF Raman response. As mentioned above, knowledge of the Raman tensor is crucial for obtaining Raman intensity. The Raman tensor for each normal mode is proportional to the change of the polarizability tensor with respect to the normal coordinates of the corresponding vibration.[92,94,155] Focusing on interlayer vibrational modes, each layer vibrates as a quasi-rigid body, and it can thus be treated as a single object. For layer 1, if the derivative of the polarizability tensor with respect to its displacement along the x direction is defined as $\overleftrightarrow{\alpha}'_{1x}$ and its displacement from the equilibrium position is Δr_{1x}, the change of the polarizability tensor for this displacement is $\overleftrightarrow{\alpha}'_{1x}\Delta r_{1x}$. Similarly, the change of the polarizability tensor by an x-direction displacement of layer 2 is $\overleftrightarrow{\alpha}'_{2x}\Delta r_{2x}$, *etc.* In a multilayer sample, the total change of the polarizability tensor is a sum of the contributions from all layers: $\Delta\overleftrightarrow{\alpha} = \sum_i \overleftrightarrow{\alpha}'_{ix}\Delta r_{ix}$. This relationship applies to shear vibrations along the x direction. Similarly for breathing vibrations along the z direction, the change of polarizability tensor is given by $\Delta\overleftrightarrow{\alpha} = \sum_i \overleftrightarrow{\alpha}'_{iz}\Delta r_{iz}$. Note that $\overleftrightarrow{\alpha}'_{ix}$, $\overleftrightarrow{\alpha}'_{iz}$ and $\Delta\overleftrightarrow{\alpha}$ are second-rank tensors, as indicated by the double arrow symbols. For the commonly used parallel polarization setup in the backscattering geometry, that is, $\overline{Z}(XX)Z$, the Raman intensity is $I \propto |\Delta\alpha_{xx}|^2$, and thus only the xx component of the tensors is needed. It follows that the total change of polarizability is $\Delta\alpha_{xx} = \sum_i \alpha'_{ix,xx}\Delta r_{ix}$ by shear vibrations, and $\Delta\alpha_{xx} = \sum_i \alpha'_{iz,xx}\Delta r_{iz}$ by breathing vibrations, respectively. Furthermore, it can be mathematically derived (see details in ref 81) that the xx component of $\overleftrightarrow{\alpha}'_{ix}$ or $\overleftrightarrow{\alpha}'_{iz}$ is related to the interlayer bond vectors in a simple fashion:

$$\alpha'_{ix,xx} = \sum_B C_{i,B}\hat{R}_{ix,B} \tag{6}$$

and

$$\alpha'_{iz,xx} = \sum_B C^*_{i,B}\hat{R}_{iz,B} \tag{7}$$

where i refers to the layer index, B indicates a bond between layer i to neighboring layer i' at equilibrium, $\vec{\hat{R}}_{i,B}$ is the corresponding normalized bond vector, and $\hat{R}_{i\mu,B}$ is its μ (=x, y, or z) component. The coefficients $C_{i,B}$ and $C^*_{i,B}$ are related to the properties of the interlayer bond B, including the interlayer bond length and the interlayer bond polarizabilities and their radial derivatives.[81,94,157−159]

In short, $\alpha'_{ix,xx}$ or $\alpha'_{iz,xx}$ can be easily obtained from the interlayer bond vectors of the system. Multiplied by the layer eigen-displacements Δr_{ix} or Δr_{iz} in eq 3, the change of the system's polarizability $\Delta\alpha_{xx}$ is obtained for the S_j or LB_j mode, which subsequently yields the Raman intensity based on $I \propto |\Delta\alpha_{xx}|^2$.[81] We will now apply this model to a few selected examples.

Trilayer Graphene. For trilayer graphene in ABA and ABC stacking polytypes, the interlayer stacking between two consecutive layers always assumes an AB arrangement, and consequently the interlayer bond length, the interlayer bond polarizabilities, and their derivatives can be considered constant,[94] which means that the coefficients $C_{i,B}$ and $C^*_{i,B}$ are constant in trilayer graphene. Therefore, eqs 6 and 7 can be simplified as $\alpha'_{ix,xx} = C\sum_B \hat{R}_{ix,B}$ and $\alpha'_{iz,xx} = C^*\sum_B \hat{R}_{iz,B}$, respectively. Figure 9a shows that for ABA stacking, the first layer only has an interlayer bond with the second layer, and the normalized bond vector is $\vec{\hat{R}}_{1,2} = (\sin\theta, 0, \cos\theta)$. The second layer has an interlayer bond with the first and third layer, and we have $\vec{\hat{R}}_{2,1} = -\vec{\hat{R}}_{1,2}$ and $\vec{\hat{R}}_{2,3} = (-\sin\theta, 0, \cos\theta)$. Finally, the third layer only develops an interlayer bond with the second layer, and we have $\vec{\hat{R}}_{3,2} = -\vec{\hat{R}}_{2,3}$. Therefore, for each layer at ABA stacking, we find[81]

$$\begin{aligned}
\alpha'_{1x,xx} &= C\hat{R}_{1x,2} = C\sin\theta = \beta\\
\alpha'_{2x,xx} &= C(\hat{R}_{2x,1} + \hat{R}_{2x,3}) = -2C\sin\theta = -2\beta\\
\alpha'_{3x,xx} &= C\hat{R}_{3x,2} = C\sin\theta = \beta
\end{aligned} \tag{8}$$

where we introduced the constant $\beta = C\sin\theta$. On the other hand, for ABC stacking, we have $\vec{\hat{R}}_{1,2} = (\sin\theta, 0, \cos\theta)$ for layer 1, $\vec{\hat{R}}_{2,1} = -\vec{\hat{R}}_{1,2}$ and $\vec{\hat{R}}_{2,3} = (\sin\theta, 0, \cos\theta)$ for layer 2, and $\vec{\hat{R}}_{3,2} = -\vec{\hat{R}}_{2,3}$ for layer 3. Therefore, for each layer in an ABC stacking:[81]

$$\begin{aligned}
\alpha'_{1x,xx} &= C\hat{R}_{1x,2} = C\sin\theta = \beta\\
\alpha'_{2x,xx} &= C(\hat{R}_{2x,1} + \hat{R}_{2x,3}) = 0\\
\alpha'_{3x,xx} &= C\hat{R}_{3x,2} = -C\sin\theta = -\beta
\end{aligned} \tag{9}$$

It is interesting to note that $\alpha'_{1x,xx} = \alpha'_{3x,xx}$ for ABA stacking as the first and third layers assume *mirror* symmetry, while $\alpha'_{1x,xx} = -\alpha'_{3x,xx}$ for ABC stacking as the first and third layers present *inversion* symmetry. In short, because the x components of the interlayer bond vectors take different values depending on the stacking type, $\alpha'_{1x,xx}$, $\alpha'_{2x,xx}$, $\alpha'_{3x,xx}$ are β, -2β, β for ABA stacking but β, 0, $-\beta$ for ABC stacking.[81,94] It follows that the change in polarizability by the shear vibrations is $\Delta\alpha_{xx} = \beta(\Delta r_{1x} - 2\Delta r_{2x} + \Delta r_{3x})$ for ABA stacking but $\Delta\alpha_{xx} = \beta(\Delta r_{1x} - \Delta r_{3x})$ for ABC stacking. Furthermore, for both stacking configurations, the

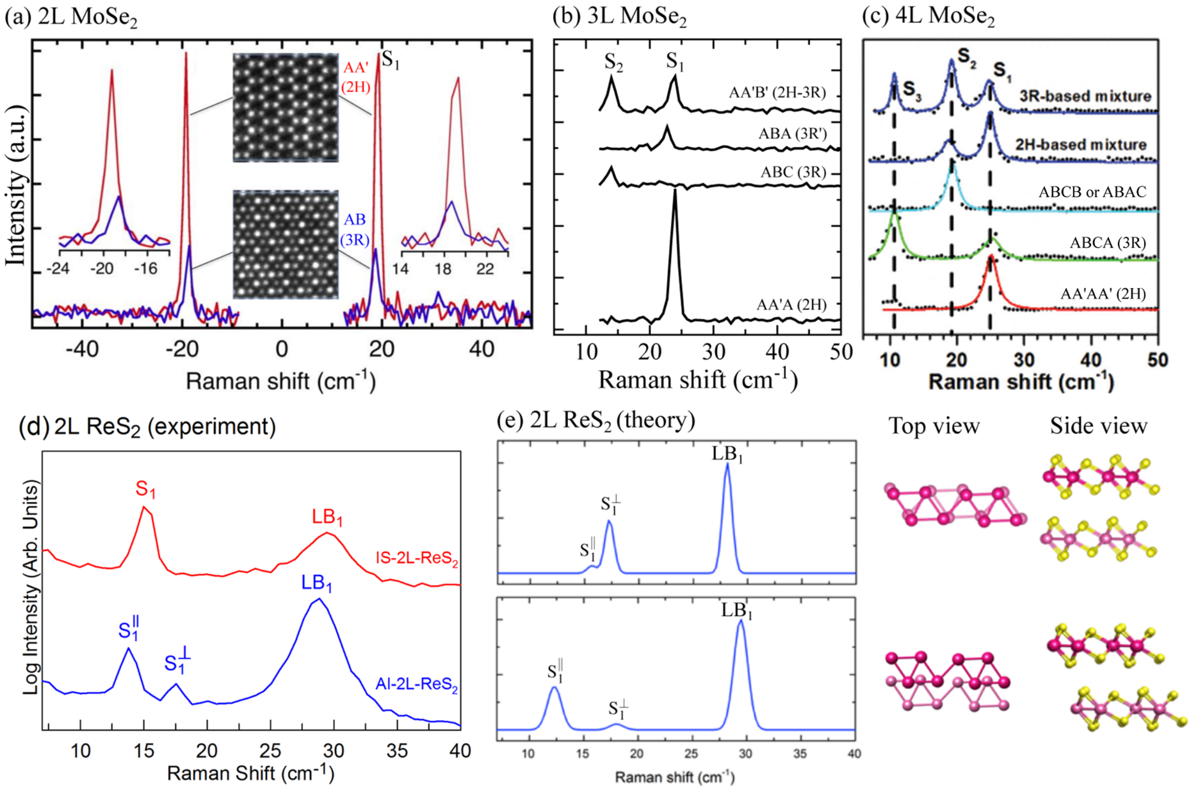

Figure 11. (a) Stokes/anti-Stokes LF Raman spectra of bilayer MoSe$_2$ with AA′ (2H) and AB (3R) stacking patterns confirmed by atomic resolution STEM. LF Raman spectra of (b) trilayer and (c) four-layer MoSe$_2$ at different stackings. (d) Experimental and (e) theoretical LF Raman spectra of bilayer ReS$_2$ for two stacking orders with the atomic structures on the right side. (a and b) Reproduced with permission from ref 52. Copyright 2015 American Chemical Society. (c) Adapted with permission from ref 75. Copyright 2015 John Wiley & Sons, Inc. (d) Reproduced with permission from ref 79. Copyright 2016 Royal Society of Chemistry. (e) Adapted with permission from ref 80. Copyright 2016 American Chemical Society.

normalized layer displacements (Δr_{1x}, Δr_{2x}, Δr_{3x}) are $\frac{1}{\sqrt{2}}(1, 0, -1)$ for the S$_2$ mode and $\frac{1}{\sqrt{1.5}}(0.5, -1, 0.5)$ for the S$_1$ mode (see Figure 10a and eq 3 from the LCM).[73,94] From these considerations, we find that

$$\Delta\alpha_{xx}(\text{ABA, S}_2) = 0; \quad \Delta\alpha_{xx}(\text{ABA, S}_1) = \sqrt{6}\beta$$
$$\Delta\alpha_{xx}(\text{ABC, S}_2) = \sqrt{2}\beta; \quad \Delta\alpha_{xx}(\text{ABC, S}_1) = 0$$

Since the Raman intensity is $I \propto |\Delta\alpha_{xx}|^2$ in a parallel polarization setup, these results can account for the fact that the S$_1$ (S$_2$) mode is observed exclusively in the Raman scattering of the ABA (ABC) stacking sequence, as discussed above in relation to Figure 10b.[73,81,94]

In contrast, the z components of the interlayer bond vectors are identical in both types of stacking orders, and it follows that $\alpha'_{1z,xx} = -\alpha'_{3z,xx} = \gamma$, while $\alpha'_{2z,xx} = 0$ for both stacking configurations. Furthermore, the layer displacements (Δr_{1z}, Δr_{2z}, Δr_{3z}) are $\frac{1}{\sqrt{2}}(1, 0, -1)$ for the LB$_2$ mode and $\frac{1}{\sqrt{1.5}}(0.5, -1, 0.5)$ for the LB$_1$ mode (Figure 10a). From this, it follows that (more details are in ref 81)

$$\Delta\alpha_{xx}(\text{ABA or ABC, LB}_2) = \sqrt{2}\gamma$$
$$\Delta\alpha_{xx}(\text{ABA or ABC, LB}_1) = 0$$

This result explains why the LB$_2$ mode is observed in both stacking configurations, while the LB$_1$ mode is not, as shown in Figure 10b.[73]

From this analysis, we conclude that the LB modes cannot be used for the effective identification of stacking order in few-layer graphene, and the focus should be on the S modes instead. Such key difference arises from the fact that the z (*i.e.*, out-of-plane) components of the interlayer bond vectors do not change for a variation in in-plane stacking, but the x (*i.e.*, in-plane) components of the interlayer bond vectors can change.[81] It is clear that by treating each layer as a single rigid object and considering only the interlayer bonds, the simple interlayer bond polarizability model offers a rich and intuitive picture of the relations between the LF Raman intensities and stacking patterns. In fact, both the model and first-principles Raman simulations[81,94] have shown that among the shear modes, the highest-frequency one S$_1$ has the largest Raman intensity in AB-stacked MLG (Figure 10c), while the lowest-frequency one S$_{N-1}$ has the largest intensity in ABC-stacked systems (Figure 10d), in agreement with recent Raman measurements.[73,74] Similar analysis can be extended to other materials in various stacking configurations to rationalize experimentally observed features, as discussed below.[81]

Group 6 TMDCs MX$_2$. Compared to MLG, the stacking situation becomes more complicated in group 6 MX$_2$ such as MoS$_2$ (Figure 9b). Unlike MLG where the interlayer stacking between adjacent layers is always of AB type, there are two distinct interlayer stacking patterns in multilayer MX$_2$, namely AA′ (2H) and AB (3R) (see the section on the unified stacking nomenclature for a reminder on notations). According to eq 6, for bilayer MX$_2$ in AA′ stacking, we find that

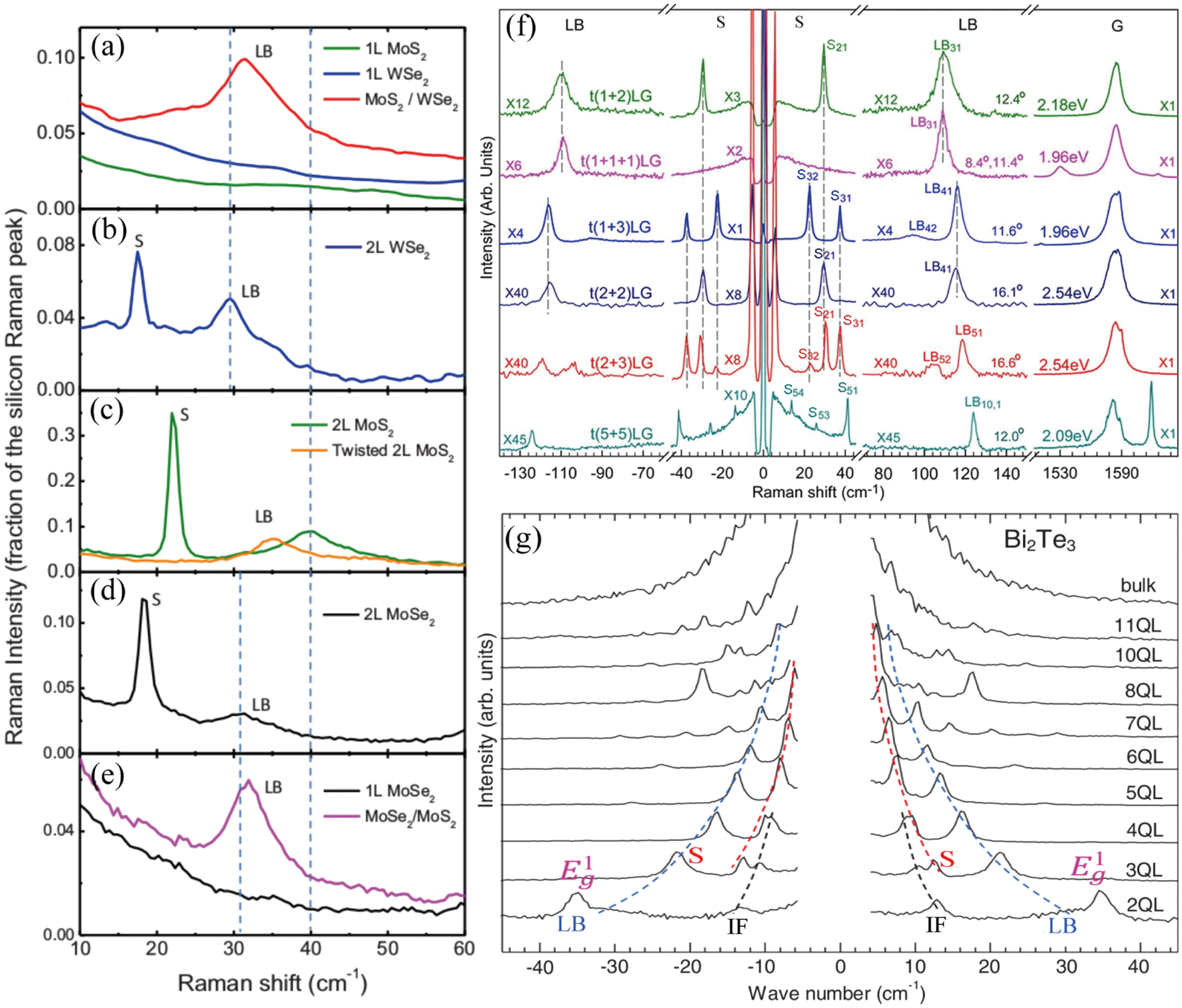

Figure 12. LF Raman spectra for (a) the MoS$_2$/WSe$_2$ heterobilayer, 1L MoS$_2$, and 1L WSe$_2$; (b) 2H-stacked 2L WSe$_2$; (c) 2H-stacked and twisted 2L MoS$_2$; (d) 2H-stacked 2L MoSe$_2$; (e) the MoSe$_2$/MoS$_2$ heterobilayer and 1L MoSe$_2$; (f) twisted MLG t(m + n)LG; and (g) Bi$_2$Te$_3$. Note that in (f), shear modes are labeled as C in some prior works. (a−e) Adapted with permission from ref 86. Copyright 2015 American Physical Society. (f) Adapted with permission from ref 83. Copyright 2015 American Chemical Society. (g) Adapted from ref 69. Copyright 2014 American Physical Society.

$$\alpha'_{1x,xx} = C_{1,2}\hat{R}_{1x,2} = C(\mathrm{AA}')\sin\theta = \beta_1$$

$$\alpha'_{2x,xx} = C_{2,1}\hat{R}_{2x,1} = -C(\mathrm{AA}')\sin\theta = -\beta_1$$

where $C_{1,2} = C_{2,1} = C(\mathrm{AA}')$ are the coefficients related to the interlayer bond polarizability and its derivatives for the AA′ stacking. For the shear mode, the normalized layer displacements $(\Delta r_{1x}, \Delta r_{2x})$ are $\frac{1}{\sqrt{2}}(1, -1)$, so the change of the polarizability is $\Delta\alpha_{xx}(\mathrm{AA}') = \sqrt{2}\ \beta_1$. Similarly, for bilayer MX$_2$ with AB stacking, we have $\Delta\alpha_{xx}(\mathrm{AB}) = \sqrt{2}\ C(\mathrm{AB})\sin\theta = \sqrt{2}\ \beta_2$, where $C(\mathrm{AB})$ is related to the interlayer bond polarizability and its derivative for AB stacking. Although the interlayer bond length is roughly the same for both AA′ and AB stacking orders, the interlayer bond polarizability and its derivatives are clearly different.[81] This has been experimentally verified by measuring the reproducible difference in LF Raman response of bilayer MX$_2$ for the two stacking orders.[52,85] Specifically, as shown in Figure 11a, Puretzky *et al.* found that the intensity of the shear mode in bilayer MoSe$_2$ drops significantly from AA′ (2H) to AB (3R) stacking,[52] thereby indicating $|\beta_1| > |\beta_2|$.

For trilayer MX$_2$, AA′A and ABA stacking orders share similar interlayer bond vectors with ABA stacking in trilayer graphene, while ABC and AA′B′ stacking orders share similar interlayer bond vectors with ABC stacking in trilayer graphene (Figure 9).[81] Similar to trilayer graphene, the normalized layer displacements $(\Delta r_{1x}, \Delta r_{2x}, \Delta r_{3x})$ are $\frac{1}{\sqrt{2}}(1, 0, -1)$ for the S$_2$ mode and $\frac{1}{\sqrt{1.5}}(0.5, -1, 0.5)$ for the S$_1$ mode. Consequently, following a similar procedure as the one used to analyze trilayer graphene, the change of polarizability due to a shear vibration for the four stacking orders in trilayer MX$_2$ can be derived as follows:[81]

$$\Delta\alpha_{xx}(\mathrm{AA'A},\ \mathrm{S}_2) = 0 \qquad \Delta\alpha_{xx}(\mathrm{AA'A},\ \mathrm{S}_1) = \sqrt{6}\beta_1$$
$$\Delta\alpha_{xx}(\mathrm{ABA},\ \mathrm{S}_2) = 0 \qquad \Delta\alpha_{xx}(\mathrm{ABA},\ \mathrm{S}_1) = \sqrt{6}\beta_2$$
$$\Delta\alpha_{xx}(\mathrm{ABC},\ \mathrm{S}_2) = \sqrt{2}\beta_2 \qquad \Delta\alpha_{xx}(\mathrm{ABC},\ \mathrm{S}_1) = 0$$
$$\Delta\alpha_{xx}(\mathrm{AA'B'},\ \mathrm{S}_2) = \sqrt{0.5}(\beta_1 + \beta_2) \qquad \Delta\alpha_{xx}(\mathrm{AA'B'},\ \mathrm{S}_1) = \sqrt{1.5}(\beta_1 - \beta_2)$$

For both AA′A (2H) and ABA (3R′) stacking orders, the S_2 peak intensity is zero, and only the S_1 mode can be observed, similar to ABA stacking in trilayer graphene. In contrast, for ABC (3R) stacking, the S_1 peak intensity is zero, and only the S_2 mode can be observed, similar to ABC stacking in trilayer graphene. The situation is different in trilayer MX_2 for the AA′B′ stacking configuration (the mixture of AA′ and AB or mixture of 2H and 3R), as both S_2 and S_1 modes have nonzero intensities. Such stacking-dependent LF Raman response obtained using the interlayer bond polarizability model explains well the experimental data of 3L $MoSe_2$ measured by Puretzky *et al.*, as shown in Figure 11b.[52] In addition, as discussed before, the fact that $|\beta_1| > |\beta_2|$ determines that the S_1 peak intensity of AA′A stacking is much higher than that of ABA stacking (Figure 11b). This feature provides a sensitive handle to differentiate between AA′A and ABA stackings as well, even though they share the same crystal symmetry.[52] Similar results have also been reported for few-layer MoS_2 and WSe_2,[52,75−78,94] suggesting that the intensities of the shear modes can be used as universal stacking fingerprints for MX_2. In contrast, the HF Raman modes do not exhibit similar discernible stacking dependence. It follows that the intensity ratios between the LF and HF modes are strongly stacking dependent as well. Since Raman intensities are sensitive to many other factors such as sample quality, laser power, substrate, *etc.*, the use of the relative intensity ratios serves as a more robust method to experimentally determine stacking configurations that does not require an explicit comparison between different stacking patterns of two or more samples.[52]

The interlayer bond polarizability model can also be extended to explain and predict stacking-dependent LF Raman signals beyond trilayer MX_2.[52,75,94] Several works[75,81,94] showed that for AA′ stacking, starting from the highest-frequency one, only S_1, S_3, S_5, ... can be observed with an intensity trend $I(S_1) > I(S_3) > I(S_5) > \ldots$ relative to each other. In fact, this trend also applies to AB and AB′ stacking types, because they share similar interlayer bond vectors according to the model.[81] For an interior layer *i*, its two interlayer bond vectors obey a relation $\hat{R}_{ix,i-1} = \hat{R}_{ix,i+1}$ in the *x* direction, which determines the value of $\alpha'_{ix,xx}$ of each layer and the intensity trend above. Indeed, one can see that for AB-stacked graphene (Figure 4), AA′-stacked MoS_2 and $MoTe_2$ (Figures 5 and 6), AB′-stacked $NbSe_2$ (Figure 8a), and AA′-stacked h-BN (Figure 8b) discussed in previous sections, the highest-frequency S branch S_1 shows the strongest intensity, followed by S_3, S_5, ... (if they are not too weak to be observed). On the contrary, for an interior layer *i* in an ABC stack, its two interlayer bond vectors obey the opposite relation $\hat{R}_{ix,i-1} = -\hat{R}_{ix,i+1}$ in the *x* direction, giving rise to dramatically different $\alpha'_{ix,xx}$ for each layer.[81] Subsequently, for ABC stacking, the trend is opposite, and starting from the lowest-frequency one, only S_{N-1}, S_{N-3}, S_{N-5}, ... can be observed with an intensity trend $I(S_{N-1}) > I(S_{N-3}) > I(S_{N-5}) > \ldots$ relative to each other. Indeed, for ABC-stacked graphene (Figure 10d), ABC-stacked $MoSe_2$ (Figure 11) and ABC-stacked Bi_2Te_3 and Bi_2Se_3 (Figure 12g), the lowest-frequency S branch S_{N-1} dominates the S peaks, followed by S_{N-3}, S_{N-5}, ... (if they are not too weak to be observed).

Clearly, the intensities of LF shear modes are sensitive to stacking orders, and the rules derived from the interlayer bond polarizability model can be generalized and are independent of the specific 2DM under investigation, thus providing useful guidelines for the determination of stacking configuration. Focusing on four-layer MX_2 as an illustrative example, we have $I(S_1) > I(S_3)$ for AA′ (2H) configuration and $I(S_3) > I(S_1)$ for ABC (3R) stacking. This simple rule enables the rapid and unequivocal determination of the high-symmetry stacking configurations (Figure 11c).[75,81] Besides AA′ (2H), AB, and ABC (3R) stackings, stacking faults and mixtures can further complicate the situation, requiring careful analysis from the interlayer bond polarizability model and DFT calculations.[12,75,81] For instance, neither AA′AA′ (2H), ABAB (3R′), nor ABCA (3R) stacking in four-layer $MoSe_2$ can lead to a strong S_2 peak as observed in Figure 11c, and instead it is a stacking fault (ABCB or ABAC, deviated from the perfect 3R or 3R′ stacking) that is responsible for the measured intensities.[75] Furthermore, the mixture of 2H and 3R stackings in 4L $MoSe_2$ can give rise to different LF Raman features, as illustrated in Figure 11c.[75] Interestingly, the ABCA (3R) and ABAC stacking sequences exhibit similar STEM signals, while their LF Raman signals are very different as illustrated in Figure 11c, indicating that in cases like this, LF Raman spectroscopy is the most suitable method to determine high-symmetry stacking configurations.[75]

Finally, we briefly discuss the general rules derived from the interlayer bond polarizability model for LB modes.[81] Unlike the case corresponding to the *x* direction, the *z* (out-of-plane) components of the interlayer bond vectors do not change when the in-plane stacking changes. It follows that for an interior layer *i* we always have $\hat{R}_{iz,i-1} = -\hat{R}_{iz,i+1}$ in the *z* direction, regardless of the stacking types. As a consequence, for all AA′, AB, AB′, and ABC stacking types, starting from the lowest-frequency one, only LB_{N-1}, LB_{N-3}, LB_{N-5}, ... can be observed with an intensity trend $I(LB_{N-1}) > I(LB_{N-3}) > I(LB_{N-5}) > \ldots$ relative to each other. This trend has been confirmed by LF Raman measurements for a broad array of 2DMs discussed in this review, including graphene, MoS_2 and $MoTe_2$, ReS_2, $NbSe_2$, PtS_2 and $PtSe_2$, Bi_2Te_3, Bi_2Se_3, *etc.*

Low-Symmetry Stacking. Moving from high-symmetry to low-symmetry stacking, a number of recent works on twisted bilayer MoS_2 and $MoSe_2$ have shown that twisting can profoundly alter the interlayer coupling, thereby notably affecting the frequencies and intensities of LF modes.[84,85] DFT modeling was used to identify five high-symmetry stacking patterns in bilayer MoS_2 and $MoSe_2$ including AB (3R) and AA at 0° and AA′ (2H), AB′, and A′B at 60°.

Simulated Raman spectra highlight notable changes in frequency and intensity for both S and LB modes between the five stacking orders.[84,85] Near 0° or 60°, where the stacking is a mixture of those high-symmetry stacking patches (forming finite-size Moiré-like patterns), minute changes in twisting can greatly modify the size of each stacking patch. The associated change in overall stacking pattern leads to strong frequency and intensity variations of LF modes as a function of twisting angle. However, when the twisting angle is near 30°, the stacking pattern shows highly mismatched lattices with no local high-symmetry domains. It follows that the interlayer coupling is nearly constant, and the frequency and intensity of LF modes are insensitive to the twisting angle. Interestingly, for bilayer $MoSe_2$, slight deviations from 60° allow for the co-existence of both high-symmetry stacking patches and mismatched regions, giving rise to two characteristic LB modes in the bilayer system. Further deviation from 60° leads to a transition to completely mismatched stacking patterns, leading to just one LB mode. Moreover, in this case the shear mode disappears because its frequency is close to zero due to the loss of the in-plane restoring force in the mismatched stacking.[80,84−86] Clearly, the non-uniform interface with variable local stacking and interlayer coupling can be probed by LF Raman spectroscopy through a careful analysis of the multiple breathing modes and the disappearance of the shear mode. In contrast, the high-frequency intralayer Raman modes exhibit much weaker dependence on the twisting angle.

In-Plane Anisotropic ReX_2. Besides the isotropic graphene and group 6 TMDCs discussed above, the stacking-dependent LF Raman response has been recently used to characterize anisotropic group 7 TMDCs such as ReS_2.[79,80,98] The additional valence electron in Re atoms (compared to Mo or W) gives rise to additional Re−Re bonds, forming zigzag-like rhenium chains with in-plane distortion.[6,160] Unlike MLG and MoS_2 where the shear modes are doubly degenerate, the degeneracy is lifted in ReS_2 owing to the in-plane anisotropy. As a result, the shear modes can be categorized into the ones vibrating parallel and the ones perpendicular to the rhenium chains.[80] For this reason, it is customary to label the two shear modes as $S_1^{\parallel}$ and $S_1^{\perp}$ in bilayer ReS_2. As shown in Figure 11d, Qiao *et al.* identified two stable stacking orders in 2L ReS_2: In the AI stacking, $S_1^{\parallel}$ and $S_1^{\perp}$ are separately resolved with a frequency difference of ~4 cm^{-1}, while in the IS stacking, they overlap to appear as a single peak S_1,[79] similar to isotropic bilayer graphene and MoS_2.[57,61,64] Because these features are not necessarily intuitive, DFT modeling played a crucial role for the understanding of such stacking-induced LF Raman behaviors. Due to the in-plane lattice distortion and low crystal symmetry, a large number of stacking configurations could be present for 2L ReS_2. By theoretically investigating possible configurations, it was possible to establish that the AI and IS stacking patterns are among the most energetically stable. More importantly, the simulated Raman spectra shown in Figure 11e confirm that for the AI stacking, $S_1^{\parallel}$ and $S_1^{\perp}$ are separated by a frequency difference well above the instrument resolution and therefore appear as two peaks.[79] This result is in stark contrast with the situation found in the IS stacking where the peaks are much closer to each other, so that only a single mixed band could be detected by Raman spectroscopy. We note that for the AI stacking, the DFT simulated Raman spectrum matches quite well with the experimental data, for both the frequencies and relative intensity (Figure 11d and 11e).[79,80] Since the energy difference between the two stacking orders is small, it is possible for the stacking to change from one into the other upon the application of an external perturbation or when the number of layers increases. The existence of this stacking polytypism contributes to resolving a number of issues related to the apparent discrepancy reported in the literature where some authors found no splitting of the shear mode or a splitting of $\lesssim$1 cm^{-1} in 2L ReS_2 (likely the IS stacking),[68,98] while others found a splitting of ~4 cm^{-1} (likely the AS stacking).[79] The two stacking orders are also present in multilayer ReS_2 samples, giving rise to different LF Raman features as well (see Figure 7).[79]

One well-suited method to verify the in-plane anisotropy of ReS_2[79] is the use of polarized Raman scattering. The S modes and LB mode show different polarization directions in AI-2L-ReS_2, while the S and LB modes show similar polarization intensity dependence in IS-2L-ReS_2. It appears that the angular dependence of the Raman intensity is not only related to the crystal orientation but also depends on the incoming photon energy.[98] This result is not really surprising since the frequency response of these materials in the presence of an external time-dependent field shows a number of sharp frequency-dependent features. Consider for example the efficiency for ReS_2 to absorb visible light: In this case the Raman tensor elements are complex, and their imaginary parts need to be considered. As a result, incident phonon energy dependence must be included when we use the angular resolved Raman spectra to identify the crystal orientation of in-plane anisotropic 2DMs. Before closing this section, we note that similar results have been observed in few-layer black phosphorus, which also shows in-plane anisotropy.[161,162]

INTERFACE IN TWO-DIMENSIONAL HETEROSTRUCTURES AND HOMOSTRUCTURES

Two-dimensional vdW heterostructures are of great fundamental interest and technological importance, as they can in principle be assembled to combine the desirable properties of individual layers into a single structure.[5,9,11,31−34] These structures can typically be fabricated either by mechanical transfer[86] or chemical growth.[87] The former technique consists in mechanically stamping one monolayer onto another. In this case, it is often difficult to control the interfacial environment and stacking order. An alternative approach is to chemically grow a monolayer onto another. This gives rise to a clean interface with a well-defined stacking configuration. As a result, the heterostructures fabricated by the two approaches exhibit different LF Raman behaviors. For instance, Lui *et al.* fabricated MoS_2/WSe_2 and $MoSe_2/MoS_2$ heterobilayers and twisted MoS_2 bilayers by mechanical transfer and investigated them by LF Raman spectroscopy as illustrated in Figure 12a−e.[86] For natural 2H-stacked (*i.e.*, Bernal stacking) 2L MoS_2, 2L WSe_2, and 2L $MoSe_2$ with commensurate crystallographic alignment, both the S and LB peaks appear. In contrast, in both MoS_2/WSe_2 and $MoSe_2/MoS_2$ heterobilayers, the LB manifests as a pronounced Raman band around 32 cm^{-1}, while the S modes cannot be seen. As the two layers are misaligned and incommensurate in the heterobilayers after the transfer process, the in-plane displacement of the two layers does not produce any overall restoring force, and the S frequency is almost zero and therefore not detected. In contrast, the out-of-plane displacement of the two layers can always create a finite restoring force regardless of the details of the in-plane stacking, leading to the appearance of the LB mode.[83−86] Similar results are found in twisted 2L MoS_2 (Figure 12c), where the stacking mismatch does not allow for the presence of a detectable shear mode. The observation of the S mode requires the commensurate stacking between the two layers, as recently reported by Zhang *et al.* in chemically grown MoS_2/WS_2 heterobilayers.[87] In this case, the epitaxial growth of MoS_2 on WS_2 enables two high-symmetry stacking orders,[87] similar to the well-known 2H and 3R stacking configurations in bilayer TMDCs discussed above. For these two commensurate stacking patterns in chemically grown MoS_2/WS_2 heterobilayers, the S Raman peak appears around 18 cm^{-1}, but disappears for the mechanically transferred heterobilayers.[87] Clearly, the presence and absence of an S mode can serve as reliable evidence of the quality of the stacking configuration in fabricated heterobilayers. In addition, the LB mode, present regardless of the details of the stacking, can be used to probe the interfacial stacking and interlayer coupling of the heterostructures. This method is very sensitive since the restoring force between two layers is a rapidly decreasing function of the layer separation. For instance, from 2H to 3R stacking in MoS_2/WS_2 heterobilayers, the LB frequency decreases by 2 cm^{-1}, due to the slightly increased interlayer distance and weakened interlayer coupling.[87] From as-grown commensurate stacking orders to as-transferred mismatch stacking orders in MoS_2/WS_2 heterobilayers, the LB frequency decreases by 2−4 cm^{-1}, suggesting weaker interlayer coupling and reduced packing efficiency.[87] Similar phenomena have been reported in TMDCs homobilayers.[52,84,85] Besides the frequency shift, the Raman intensity of the LB modes can also be helpful to examine the quality of the interface. For instance, a nonuniform interface can be formed in an unannealed MoS_2/WSe_2 heterobilayer sample after mechanical transfer, where local regions with shorter interlayer separations have stronger interlayer coupling, and thus a stronger LB intensity. Using Raman mapping, the spatial distribution of the LB mode intensity shows a higher sensitivity to the quality of the interface compared to a photoluminescence mapping. For example, the LB mode can only be detected in the heterostructure regions with direct interlayer contact and an atomically clean interface.[86]

LF Raman spectroscopy can also be applied to study the interfacial coupling and lattice dynamics of vdW heterostructures formed by two different types of 2DMs, such as semimetals and semiconductors. For example, a series of additional LB modes with frequencies dependent on the number of layers have been observed by transferring MoS_2 flakes onto graphene flakes with appropriate annealing process to form graphene/MoS_2 heterostructures.[163] The interfacial breathing force constant between MoS_2 and graphene is comparable with that of multilayer MoS_2 and graphene. Therefore, LF Raman spectroscopy can be utilized to characterize the interfacial quality of graphene-based devices, where graphene flake is used as an electrode and also introduces a barrier, and to measure the interfacial interactions in various heterostructures for further engineering the heterostructures-based electronic and photonic devices.

Twisted Multilayer Graphene. Twisted MLG is another form of vdW heterostructure that shows interesting LF Raman response governed by the details of the interface. In twisted $(m + n)$-layer graphene (t$(m + n)$LG), such as artificially assembled or CVD grown m-layer graphene (mLG) on top of n-layer graphene (nLG), the mLG and nLG are twisted by an angle θ relative to each other.[43,82,83,164−166] Strictly speaking, the t$(m + n)$LG is a type of heterostructure since the assembly proceeds between two distinct subsystems. Here, we focus our attention on the LF Raman resonance spectra of t$(m + n)$LG. The optical and electronic properties of t$(m + n)$LG can be tuned by changing θ and can result in the emergence of a number of properties in addition to those found in high-symmetry ABA- and ABC-stacked graphene (Figure 12f).[41,167,168] In contrast to the weak S and LB modes in high-symmetry stacked graphene, the intensities of the S and LB modes in t$(m + n)$LG are greatly enhanced under specific excitation energies due to resonance with an additional optically allowed electronic transition.[43,82,83,164,169] In particular, these transition energies are determined by the twisting angle θ.[43,83,141,164] Furthermore, the S and LB modes also show different behaviors in t$(m + n)$LG. The S modes always arise from mL and nL AB-stacked graphene (*i.e.*, the individual subsystems with high-symmetry stacking). The twisted interface with misaligned lattices does not produce any observable S mode, as its frequency is close to zero. Thus, there are $n + m - 2$ S modes in t$(m + n)$LG,[83,164−166] and their frequencies are slightly affected by the twisted interface due to the weak interface coupling. For example, in t(1 + 2)LG, one can only observe the $S_{2,1}$ mode around 30 cm^{-1}, which is close to the frequency 32 cm^{-1} of AB-stacked 2L graphene. Similarly, with t(2 + 3)LG, the $S_{2,1}$, $S_{3,1}$, and $S_{3,2}$ modes are also observed as shown in Figure 12f. While the LB modes in t$(m + n)$LG are consistent with those of the N ($N = m + n$) AB-stacked graphene. These modes are determined by the total number of layers N but are independent of the twisting angle θ, because the frequencies of the out-of-plane LB modes are generally insensitive to the in-plane stacking variation with the twisting angle.[83,164−166] For example, in t(1 + 1 + 1)LG and t(1 + 2)LG, one LB mode at 109 and 110 cm^{-1} is observed, respectively. The frequencies of LB modes in t$(m + n)$LG can be well reproduced by the LCM using a next-nearest-neighbor approximation.[83,164,166] These different behaviors of S and LB modes in t$(m + n)$LG are due to the in-plane periodicity mismatch at the twisted interface.[83] In addition, CVD-grown MLG (CVD-MLG) flakes usually consist of multiple single crystal domains, whose stacking orders can be quite diverse due to the various choices of layer number, stacking sequence, and twist angle.[165] LB modes are almost independent of the details of stacking but are ideal to determine the number of layers in CVD-MLG flakes. Conversely, since S modes are sensitive to the stacking details, the stacking sequence of a CVD-MLG flake can be determined by the S modes.[165]

Interaction with a Substrate. Besides the LF Raman modes arising from within 2DMs, additional interlayer vibrations could, in principle, also emerge from the interaction between 2DMs and substrate. For example, Zhao *et al.* observed an intense ultralow (<12 cm^{-1}) frequency peak in 2−4 quintuple-layer (QL) Bi_2Te_3 deposited on a substrate, which was tentatively attributed to a substrate-induced interface mode (labeled as IF in Figure 12g).[69] Although its origin is not entirely clear, it might involve the out-of-phase displacements between Bi_2Te_3 and the substrate, according to a version of the LCM theory including a substrate. The measured frequency is below the S and LB bands that are intrinsic to Bi_2Te_3. This mode is sensitive to the choice of the substrate and could be used to probe the interface between 2DMs and substrates. Note that a number of studies have unsuccessfully attempted to demonstrate the presence of this interface-induced signature in LF Raman spectra in TMDCs.[96] The absence of such a signature can be due to a number of effects, including a nonuniform interface, weak coupling, and intensity below instrumental detection limit.

SUMMARY AND OUTLOOK

Experimental Perspective. This review provides ample evidence that LF Raman spectra not only can be used as a highly sensitive indicator for determining the number of layers in few-layer 2DMs but also can be employed to describe stacking orders and interlayer coupling. With the increasing number of few-layer 2DMs and the even larger number of possible heterostructures involving combinations of them, ultralow frequency Raman spectroscopy will play a central role in their characterization. Such characterization is crucial as exemplified by the emerging properties in these structures. For instance, the monolayer and few-layer ferromagnetic CrI_3 and $Cr_2Ge_2Te_6$ show a significantly different behavior compared to their bulk counterparts.[170,171] As another example, heterostructures based on ferromagnetic materials such as WSe_2/CrI_3 strongly affect the valley polarization of WSe_2.[172] In order to understand how the interlayer coupling impacts the physical properties of ferromagnetic materials and related heterostructures, further experimental and theoretical studies are needed in which LF Raman spectroscopy is expected to be an important tool to detect emerging two-dimensional materials and related heterostructures. In addition, LF Raman spectroscopy can be used to explore how layer–layer vibrations couple with intralayer exciton transitions by exploiting resonant Raman scattering. For example, in few-layer WS_2, besides the S and LB modes, when the excitation energies are close to the B(A) exciton transitions, two additional Raman modes (TA, LA) that are independent of the number of layers and excitation energies are also observed.[130] Those modes may originate from the acoustic phonons near the Γ point.[130] When the excitation energies are slightly lower than the A exciton transitions, the lowest-frequency S modes show a Fano line shape, which is due to quantum interference between a discrete S phonon and a continuum of dark A excitonic states. Moreover, many Raman forbidden phonon modes can also be observed due to dark exciton resonance Raman scattering, in which the dipole-transition parity selection rules are met when the forbidden phonon is resonantly scattered by dark excitons.[130] Therefore, LF Raman spectroscopy provides a great opportunity to simultaneously probe the dark excitons, Fano resonance, forbidden phonons, and electron–phonon many-body effects in multilayer 2DMs.

As discussed in this review, the VBG-based notch filter makes it possible to measure LF Raman modes down to 2 cm^{-1} at certain laser wavelengths[103] (such as 488 nm), thus providing an opportunity to study Brillouin scattering from acoustic phonon of 2DMs and other quasi-particles such as magnons in layered antiferromagnetic materials and related heterostructures. Although VBG-based LF Raman spectrometer has many advantages, there are still a few problems to be solved. First, it is costly to achieve multiwavelength Raman measurements with VBG-based single monochromator spectrometers, because each set of VBG filters only works for one excitation wavelength. Second, the optical density and narrow bandwidth of an individual VBG-based notch filter need to be improved to speed up its operational rate for LF Raman measurements. Third, limited by dielectric materials, the VBG-based LF Raman measurements using excitation wavelengths below 350 nm are still not available thus far. Therefore, the triple monochromator Raman system with a subtractive mode configuration remains a good choice for LF Raman measurements using excitation wavelengths in the ultraviolet range. In addition, owing to its high throughput and the ease of its operation, edge filter is widely used in single monochromator Raman systems. The technical improvement of the edge filter makes the LF Raman signal down to 10 cm^{-1} detectable but commercial high-quality ultrasteep edge filter below 10 cm^{-1} would be desirable for routine test of LF Raman signals.

Theoretical Perspective. The simple LCM provides a fairly accurate picture of the thickness dependence of the LF modes frequencies and is also a powerful tool to study the interlayer coupling strength.[57] As each layer can be treated as a single object in the interlayer vibrations, the LCM is in principle valid for any two-dimensional layered materials. Additionally, the LCM can be extended to include the second or third nearest-neighbor interactions to yield quantitative agreement with experiment.[83] Meanwhile, first-principles DFT simulations also offer invaluable information about LF Raman modes and interlayer coupling in 2DMs. However, DFT still faces a great challenge when it comes to the degree of accuracy it can achieve. The frequencies of LF modes are almost solely determined by the interlayer restoring forces, and thus accurate capture of the interlayer interactions is essential. For graphene and MoS_2, the interlayer coupling is mainly of vdW type, but for many recently explored 2DMs like black phosphorus and PtS_2, a strong degree of electronic hybridization and covalent bonding between layers is present, giving rise to complex interlayer coupling.[137,138] The vdW functionals currently available do not seem sufficient to describe the complexity of interlayer interactions, and different 2DMs often rely on different vdW functionals used in DFT to yield best calculated frequencies. In many cases, the best agreement with experiment is often achieved using the local density functional (LDA) approximation.[52,57,64] This is due to the fortuitous cancellation between LDA's lack of description of the vdW interaction (which is purely nonlocal) and its overestimating tendency of the covalent bonding between layers. Therefore, further improvement on functionals is needed for DFT to accurately describe the complex interlayer coupling and the frequencies of LF modes. Another important issue to be addressed is the anharmonic scattering of LF modes. The LCM and most of DFT phonon calculations are based on the harmonic approximation, but LF Raman measurements sometimes find strong anharmonic broadening and shifts for LF modes. For example, the LB modes in many TMDCs (particularly for the bilayers) are much more broadened and weakened compared to the S modes (see Figure 5), owing to larger phonon–phonon scattering.[52,61,63,64] It follows that anharmonic effects, including 3-phonon, 4-phonon, *etc.* and thermal-expansion contributions, need to be considered for accurate phonon calculations.[173,174]

As for the Raman intensities of LF modes, the interlayer bond polarizability model, that simplifies each layer as a single object and only considers interlayer bond vectors and bond polarizabilities, serves as a simple yet powerful approach to explain and predict stacking-dependent LF Raman signals.[81,94] In this review, we have shown its validity for a broad array of 2DMs in diverse stacking configurations and highlighted general rules regarding how LF Raman intensities depend on stacking patterns. However, further developments of the model are required to extend its applicability to nontrivial stacking orders in low-symmetry anisotropic 2DMs such as ReS_2 and black phosphorus. On the other hand, DFT calculations provide a direct approach to study the relations between LF

Raman intensities and stacking configurations, which proves particularly useful for low-symmetry stacking configurations in twisted samples and low-symmetry materials such as ReS_2.[80,84,85] In spite of the reported success of DFT-based modeling, the theoretical and experimental Raman intensities of LF modes are often in qualitative or, at best, semiquantitative agreement. A key reason is that very often nonresonant Raman intensities (*i.e*, corresponding to zero photon energy) are calculated, but intensities are in fact strongly dependent on the laser photon energy.[175] A few recent works on HF modes indicate that a better agreement can be achieved if intensities are computed at the laser energy.[176−178] It is expected that resonant Raman simulations of LF modes will also improve the agreement with experiment, and thus more efforts should be devoted to this research direction.

AUTHOR INFORMATION

Corresponding Authors

*E-mail: phtan@semi.ac.cn.

*E-mail: meuniv@rpi.edu.

ORCID

Jun Zhang: 0000-0002-9831-6796

Bobby G. Sumpter: 0000-0001-6341-0355

Ping-Heng Tan: 0000-0001-6575-1516

Vincent Meunier: 0000-0002-7013-179X

Author Contributions

⊥These authors contributed equally to this work.

Notes

This manuscript has been authored by UT-Battelle, LLC under contract no. DE-AC05-00OR22725 with the U.S. Department of Energy. The United States Government retains and the publisher, by accepting the article for publication, acknowledges that the United States Government retains a nonexclusive, paid-up, irrevocable, worldwide license to publish or reproduce the published form of this manuscript, or allow others to do so, for United States Government purposes. The Department of Energy will provide public access to these results of federally sponsored research in accordance with the DOE Public Access Plan (http://energy.gov/downloads/doe-public-access-plan).

The authors declare no competing financial interest.

ACKNOWLEDGMENTS

L.L. was supported by Eugene P. Wigner Fellowship at Oak Ridge National Laboratory. L.L. and B.G.S. acknowledge work at the Center for Nanophase Materials Sciences, which is a DOE Office of Science User Facility. J.Z. and P.T. acknowledge support from the National Key Research and Development Program of China (2016YFA0301200,2017YFA0303401), NSFC (11574305, 51527901, 11474277, and 11434010), the Key Research Program of the Chinese Academy of Sciences (grant nos. XDPB0602 and XDPB08-2), and Beijing Municipal Science and Technology Commission. J.Z. also acknowledges support from National Young 1000 Talent Plan of China. V.M. acknowledges the support by NSF grant EFRI 2-DARE (EFRI-1542707) and by the Office of Naval Research.

VOCABULARY:

two-dimensional materials, materials characterized by feature size significantly smaller than a few nanometers in one spatial dimension; **(ultra) low-frequency Raman spectroscopy**, Raman scattering with hardware upgrades designed to probe vibrational modes with frequencies typically below 100 cm^{-1}; **shear mode**, a low-frequency layer−layer vibration characteristic of layered materials where the atomic motions consist of quasi-rigid lateral motions of the individual layers; **layer-breathing mode**, a low-frequency layer−layer vibration characteristic of layered materials where the atomic motions consist of quasi-rigid motions of the individual layers along the normal of each layer; **linear chain model**, a one-dimensional ball-and-spring model that treats an entire layer in two-dimensional materials as a single ball and the interlayer coupling as a harmonic spring; **interlayer bond polarizability model**, an approximation that includes the changes in polarizability from interlayer bonds and neglects contributions from in-plane chemical bonds to simplify the computation of Raman intensities of interlayer vibrational modes.

REFERENCES

(1) Novoselov, K.; Geim, A.; Morozov, S.; Jiang, D.; Zhang, Y.; Dubonos, S.; Grigorieva, I.; Firsov, A. Electric Field Effect in Atomically Thin Carbon Films. *Science* **2004**, *306*, 666−669.

(2) Novoselov, K.; Neto, A. C. Two-Dimensional Crystals-Based Heterostructures: Materials with Tailored Properties. *Phys. Scr.* **2012**, *2012*, 014006.

(3) Wilson, J.; Yoffe, A. The Transition Metal Dichalcogenides Discussion and Interpretation of the Observed Optical, Electrical and Structural Properties. *Adv. Phys.* **1969**, *18*, 193−335.

(4) Radisavljevic, B.; Radenovic, A.; Brivio, J.; Giacometti, V.; Kis, A. Single-Layer MoS_2 Transistors. *Nat. Nanotechnol.* **2011**, *6*, 147−150.

(5) Butler, S. Z.; Hollen, S. M.; Cao, L.; Cui, Y.; Gupta, J. A.; Gutierrez, H. R.; Heinz, T. F.; Hong, S. S.; Huang, J.; Ismach, A. F.; Johnston-Halperin, E.; Kuno, M.; Plashnitsa, V. V.; Robinson, R. D.; Ruoff, R. S.; Salahuddin, S.; Shan, J.; Shi, L.; Spencer, M. G.; Terrones, M.; et al. Progress, Challenges, and Opportunities in Two-Dimensional Materials Beyond Graphene. *ACS Nano* **2013**, *7*, 2898−2926.

(6) Tongay, S.; Sahin, H.; Ko, C.; Luce, A.; Fan, W.; Liu, K.; Zhou, J.; Huang, Y.-S.; Ho, C.-H.; Yan, J.; Ogletree, D. F.; Aloni, S.; Ji, J.; Li, S.; Li, J.; Peeters, F. M.; Wu, J. Monolayer Behaviour in Bulk ReS_2 Due to Electronic and Vibrational Decoupling. *Nat. Commun.* **2014**, *5*, 3252.

(7) Bonaccorso, F.; Tan, P.-H.; Ferrari, A. C. Multiwall Nanotubes, Multilayers, and Hybrid Nanostructures: New Frontiers for Technology and Raman Spectroscopy. *ACS Nano* **2013**, *7*, 1838−1844.

(8) Chhowalla, M.; Shin, H. S.; Eda, G.; Li, L.-J.; Loh, K. P.; Zhang, H. The Chemistry of Two-Dimensional Layered Transition Metal Dichalcogenide Nanosheets. *Nat. Chem.* **2013**, *5*, 263−275.

(9) Bhimanapati, G. R.; Lin, Z.; Meunier, V.; Jung, Y.; Cha, J.; Das, S.; Xiao, D.; Son, Y.; Strano, M. S.; Cooper, V. R.; Liang, L.; Louie, S. G.; Ringe, E.; Zhou, W.; Kim, S. S.; Naik, R. R.; Sumpter, B. G.; Terrones, H.; Xia, F.; Wang, Y.; et al. Recent Advances in Two-Dimensional Materials Beyond Graphene. *ACS Nano* **2015**, *9*, 11509−11539.

(10) Zhang, X.; Qiao, X.-F.; Shi, W.; Wu, J.-B.; Jiang, D.-S.; Tan, P.-H. Phonon and Raman Scattering of Two-Dimensional Transition Metal Dichalcogenides from Monolayer, Multilayer to Bulk Material. *Chem. Soc. Rev.* **2015**, *44*, 2757−2785.

(11) Zhang, X.; Tan, Q.-H.; Wu, J.-B.; Shi, W.; Tan, P.-H. Review on the Raman Spectroscopy of Different Types of Layered Materials. *Nanoscale* **2016**, *8*, 6435−6450.

(12) Lu, X.; Luo, X.; Zhang, J.; Quek, S. Y.; Xiong, Q. Lattice Vibrations and Raman Scattering in Two-Dimensional Layered Materials Beyond Graphene. *Nano Res.* **2016**, *9*, 3559−3597.

(13) Oyedele, A. D.; Yang, S.; Liang, L.; Puretzky, A. A.; Wang, K.; Zhang, J.; Yu, P.; Pudasaini, P. R.; Ghosh, A. W.; Liu, Z.; Rouleau, C. M.; Sumpter, B. G.; Chisholm, M. F.; Zhou, W.; Rack, P. D.; Geohegan, D. B.; Xiao, K. $PdSe_2$: Pentagonal Two-Dimensional Layers with High Air Stability for Electronics. *J. Am. Chem. Soc.* **2017**, *139*, 14090−14097.

(14) Li, L.; Yu, Y.; Ye, G. J.; Ge, Q.; Ou, X.; Wu, H.; Feng, D.; Chen, X. H.; Zhang, Y. Black Phosphorus Field-Effect Transistors. *Nat. Nanotechnol.* **2014**, *9*, 372−377.

(15) Liu, H.; Neal, A. T.; Zhu, Z.; Luo, Z.; Xu, X.; Tománek, D.; Ye, P. D. Phosphorene: An Unexplored 2D Semiconductor with a High Hole Mobility. *ACS Nano* **2014**, *8*, 4033−4041.

(16) Xia, F.; Wang, H.; Jia, Y. Rediscovering Black Phosphorus As an Anisotropic Layered Material for Optoelectronics and Electronics. *Nat. Commun.* **2014**, *5*, 4458.

(17) Wood, J. D.; Wells, S. A.; Jariwala, D.; Chen, K.-S.; Cho, E.; Sangwan, V. K.; Liu, X.; Lauhon, L. J.; Marks, T. J.; Hersam, M. C. Effective Passivation of Exfoliated Black Phosphorus Transistors Against Ambient Degradation. *Nano Lett.* **2014**, *14*, 6964−6970.

(18) Liang, L.; Wang, J.; Lin, W.; Sumpter, B. G.; Meunier, V.; Pan, M. Electronic Bandgap and Edge Reconstruction in Phosphorene Materials. *Nano Lett.* **2014**, *14*, 6400−6406.

(19) Ling, X.; Liang, L.; Huang, S.; Puretzky, A. A.; Geohegan, D. B.; Sumpter, B. G.; Kong, J.; Meunier, V.; Dresselhaus, M. S. Low-Frequency Interlayer Breathing Modes in Few-Layer Black Phosphorus. *Nano Lett.* **2015**, *15*, 4080−4088.

(20) Ling, X.; Wang, H.; Huang, S.; Xia, F.; Dresselhaus, M. S. The Renaissance of Black Phosphorus. *Proc. Natl. Acad. Sci. U. S. A.* **2015**, *112*, 4523−4530.

(21) Kang, J.; Wood, J. D.; Wells, S. A.; Lee, J.-H.; Liu, X.; Chen, K.-S.; Hersam, M. C. Solvent Exfoliation of Electronic-Grade, Two-Dimensional Black Phosphorus. *ACS Nano* **2015**, *9*, 3596−3604.

(22) Aufray, B.; Kara, A.; Vizzini, S.; Oughaddou, H.; Leandri, C.; Ealet, B.; Le Lay, G. Graphene-like Silicon Nanoribbons on Ag (110): A Possible Formation of Silicene. *Appl. Phys. Lett.* **2010**, *96*, 183102.

(23) Fleurence, A.; Friedlein, R.; Ozaki, T.; Kawai, H.; Wang, Y.; Yamada-Takamura, Y. Experimental Evidence for Epitaxial Silicene on Diboride Thin Films. *Phys. Rev. Lett.* **2012**, *108*, 245501.

(24) Vogt, P.; De Padova, P.; Quaresima, C.; Avila, J.; Frantzeskakis, E.; Asensio, M. C.; Resta, A.; Ealet, B.; Le Lay, G. Silicene: Compelling Experimental Evidence for Graphenelike Two-Dimensional Silicon. *Phys. Rev. Lett.* **2012**, *108*, 155501.

(25) Tao, L.; Cinquanta, E.; Chiappe, D.; Grazianetti, C.; Fanciulli, M.; Dubey, M.; Molle, A.; Akinwande, D. Silicene Field-Effect Transistors Operating at Room Temperature. *Nat. Nanotechnol.* **2015**, *10*, 227−231.

(26) Bianco, E.; Butler, S.; Jiang, S.; Restrepo, O. D.; Windl, W.; Goldberger, J. E. Stability and Exfoliation of Germanane: A Germanium Graphane Analogue. *ACS Nano* **2013**, *7*, 4414−4421.

(27) Dávila, M.; Xian, L.; Cahangirov, S.; Rubio, A.; Le Lay, G. Germanene: ANovel Two-Dimensional Germanium Allotrope Akin to Graphene and Silicene. *New J. Phys.* **2014**, *16*, 095002.

(28) Jiang, S.; Butler, S.; Bianco, E.; Restrepo, O. D.; Windl, W.; Goldberger, J. E. Improving the Stability and Optical Properties of Germanane *Via* One-Step Covalent Methyl-Termination. *Nat. Commun.* **2014**, *5*, 3389.

(29) Zhu, F.-f.; Chen, W.-j.; Xu, Y.; Gao, C.-l.; Guan, D.-d.; Liu, C.-h.; Qian, D.; Zhang, S.-C.; Jia, J.-f Epitaxial Growth of Two-Dimensional Stanene. *Nat. Mater.* **2015**, *14*, 1020−1025.

(30) Mannix, A. J.; Zhou, X.-F.; Kiraly, B.; Wood, J. D.; Alducin, D.; Myers, B. D.; Liu, X.; Fisher, B. L.; Santiago, U.; Guest, J. R.; Yacaman, M. J.; Ponce, A.; Oganov, A. R.; Hersam, M. C.; Guisinger, N. P. Synthesis of Borophenes: Anisotropic, Two-Dimensional Boron Polymorphs. *Science* **2015**, *350*, 1513−1516.

(31) Ferrari, A. C.; Basko, D. M. Raman Spectroscopy As a Versatile Tool for Studying the Properties of Graphene. *Nat. Nanotechnol.* **2013**, *8*, 235−246.

(32) Lee, C.-H.; Lee, G.-H.; van der Zande, A. M.; Chen, W.; Li, Y.; Han, M.; Cui, X.; Arefe, G.; Nuckolls, C.; Heinz, T. F.; Guo, J.; Hone, J.; Kim, P. Atomically Thin P-N Junctions with van der Waals Heterointerfaces. *Nat. Nanotechnol.* **2014**, *9*, 676−681.

(33) Hong, X.; Kim, J.; Shi, S.-F.; Zhang, Y.; Jin, C.; Sun, Y.; Tongay, S.; Wu, J.; Zhang, Y.; Wang, F. Ultrafast Charge Transfer in Atomically Thin MoS_2/WS_2 Heterostructures. *Nat. Nanotechnol.* **2014**, *9*, 682−686.

(34) Ceballos, F.; Bellus, M. Z.; Chiu, H.-Y.; Zhao, H. Ultrafast Charge Separation and Indirect Exciton Formation in a MoS_2-$MoSe_2$ van der Waals Heterostructure. *ACS Nano* **2014**, *8*, 12717−12724.

(35) Deng, Y.; Luo, Z.; Conrad, N. J.; Liu, H.; Gong, Y.; Najmaei, S.; Ajayan, P. M.; Lou, J.; Xu, X.; Ye, P. D. Black Phosphorus-Monolayer MoS_2 van der Waals Heterojunction P-N Diode. *ACS Nano* **2014**, *8*, 8292−8299.

(36) Splendiani, A.; Sun, L.; Zhang, Y.; Li, T.; Kim, J.; Chim, C.-Y.; Galli, G.; Wang, F. Emerging Photoluminescence in Monolayer MoS_2. *Nano Lett.* **2010**, *10*, 1271−1275.

(37) Mak, K. F.; Lee, C.; Hone, J.; Shan, J.; Heinz, T. F. Atomically Thin MoS_2: A New Direct-Gap Semiconductor. *Phys. Rev. Lett.* **2010**, *105*, 136805.

(38) Tran, V.; Soklaski, R.; Liang, Y.; Yang, L. Layer-Controlled Band Gap and Anisotropic Excitons in Few-Layer Black Phosphorus. *Phys. Rev. B: Condens. Matter Mater. Phys.* **2014**, *89*, 235319.

(39) Geim, A.; Grigorieva, I. van der Waals Heterostructures. *Nature* **2013**, *499*, 419−425.

(40) Dean, C. R.; Wang, L.; Maher, P.; Forsythe, C.; Ghahari, F.; Gao, Y.; Katoch, J.; Ishigami, M.; Moon, P.; Koshino, M.; Taniguchi, T.; Watanabe, K.; Shepard, K. L.; Hone, J.; Kim, P. Hofstadter's Butterfly and the Fractal Quantum Hall Effect in Moire Superlattices. *Nature* **2013**, *497*, 598−602.

(41) Li, G.; Luican, A.; dos Santos, J. L.; Neto, A. C.; Reina, A.; Kong, J.; Andrei, E. Observation of van Hove Singularities in Twisted Graphene Layers. *Nat. Phys.* **2010**, *6*, 109−113.

(42) Jiang, T.; Liu, H.; Huang, D.; Zhang, S.; Li, Y.; Gong, X.; Shen, Y.-R.; Liu, W.-T.; Wu, S. Valley and Band Structure Engineering of Folded MoS_2 Bilayers. *Nat. Nanotechnol.* **2014**, *9*, 825−829.

(43) Wu, J.-B.; Zhang, X.; Ijäs, M.; Han, W.-P.; Qiao, X.-F.; Li, X.-L.; Jiang, D.-S.; Ferrari, A. C.; Tan, P.-H. Resonant Raman Spectroscopy of Twisted Multilayer Graphene. *Nat. Commun.* **2014**, *5*, 5309.

(44) Zhang, L.; Zhang, Y.; Camacho, J.; Khodas, M.; Zaliznyak, I. The Experimental Observation of Quantum Hall Effect of L= 3 Chiral Quasiparticles in Trilayer Graphene. *Nat. Phys.* **2011**, *7*, 953−957.

(45) Lui, C. H.; Li, Z.; Mak, K. F.; Cappelluti, E.; Heinz, T. F. Observation of an Electrically Tunable Band Gap in Trilayer Graphene. *Nat. Phys.* **2011**, *7*, 944−947.

(46) Bao, W.; Jing, L.; Velasco, J., Jr; Lee, Y.; Liu, G.; Tran, D.; Standley, B.; Aykol, M.; Cronin, S. B.; Smirnov, D.; Koshino, M.; McCann, E.; Bockrath, M.; Lau, C. N. Stacking-Dependent Band Gap and Quantum Transport in Trilayer Graphene. *Nat. Phys.* **2011**, *7*, 948−952.

(47) Morpurgo, A. F. Ten Years of Nature Physics: The ABC of 2D Materials. *Nat. Phys.* **2015**, *11*, 625−626.

(48) Suzuki, R.; Sakano, M.; Zhang, Y. J.; Akashi, R.; Morikawa, D.; Harasawa, A.; Yaji, K.; Kuroda, K.; Miyamoto, K.; Okuda, T.; Ishizaka, K.; Arita, R.; Iwasa, Y. Valley-Dependent Spin Polarization in Bulk MoS_2 with Broken Inversion Symmetry. *Nat. Nanotechnol.* **2014**, *9*, 611−617.

(49) van der Zande, A. M.; Kunstmann, J.; Chernikov, A.; Chenet, D. A.; You, Y.; Zhang, X.; Huang, P. Y.; Berkelbach, T. C.; Wang, L.; Zhang, F.; Hybertsen, M. S.; Muller, D. A.; Reichman, D. R.; Heinz, T. F.; Hone, J. C. Tailoring the Electronic Structure in Bilayer Molybdenum Disulfide *Via* Interlayer Twist. *Nano Lett.* **2014**, *14*, 3869−3875.

(50) Huang, S.; Ling, X.; Liang, L.; Kong, J.; Terrones, H.; Meunier, V.; Dresselhaus, M. S. Probing the Interlayer Coupling of Twisted Bilayer MoS_2 Using Photoluminescence Spectroscopy. *Nano Lett.* **2014**, *14*, 5500−5508.

(51) Liu, K.; Zhang, L.; Cao, T.; Jin, C.; Qiu, D.; Zhou, Q.; Zettl, A.; Yang, P.; Louie, S. G.; Wang, F. Evolution of Interlayer Coupling in Twisted Molybdenum Disulfide Bilayers. *Nat. Commun.* **2014**, *5*, 4966.

(52) Puretzky, A. A.; Liang, L.; Li, X.; Xiao, K.; Wang, K.; Mahjouri-Samani, M.; Basile, L.; Idrobo, J. C.; Sumpter, B. G.; Meunier, V.; Geohegan, D. B. Low-Frequency Raman Fingerprints of Two-Dimensional Metal Dichalcogenide Layer Stacking Configurations. *ACS Nano* **2015**, *9*, 6333−6342.

(53) Li, X.-L.; Han, W.-P.; Wu, J.-B.; Qiao, X.-F.; Zhang, J.; Tan, P.-H. Layer-Number Dependent Optical Properties of 2D Materials and Their Application for Thickness Determination. *Adv. Funct. Mater.* **2017**, *27*, 1604468.

(54) Lee, C.; Yan, H.; Brus, L. E.; Heinz, T. F.; Hone, J.; Ryu, S. Anomalous Lattice Vibrations of Single- and Few-Layer MoS_2. *ACS Nano* **2010**, *4*, 2695−2700.

(55) Lu, W.; Nan, H.; Hong, J.; Chen, Y.; Zhu, C.; Liang, Z.; Ma, X.; Ni, Z.; Jin, C.; Zhang, Z. Plasma-Assisted Fabrication of Monolayer Phosphorene and Its Raman Characterization. *Nano Res.* **2014**, *7*, 853−859.

(56) Ji, J.; Dong, S.; Zhang, A.; Zhang, Q. Low-Frequency Interlayer Vibration Modes in Two-Dimensional Layered Materials. *Phys. E* **2016**, *80*, 130−141.

(57) Tan, P. H.; Han, W. P.; Zhao, W. J.; Wu, Z. H.; Chang, K.; Wang, H.; Wang, Y. F.; Bonini, N.; Marzari, N.; Pugno, N.; Savini, G.; Lombardo, A.; Ferrari, A. C. The Shear Mode of Multilayer Graphene. *Nat. Mater.* **2012**, *11*, 294−300.

(58) Lui, C. H.; Malard, L. M.; Kim, S.; Lantz, G.; Laverge, F. E.; Saito, R.; Heinz, T. F. Observation of Layer-Breathing Mode Vibrations in Few-Layer Graphene Through Combination Raman Scattering. *Nano Lett.* **2012**, *12*, 5539−5544.

(59) Lui, C. H.; Heinz, T. F. Measurement of Layer Breathing Mode Vibrations in Few-Layer Graphene. *Phys. Rev. B: Condens. Matter Mater. Phys.* **2013**, *87*, 121404.

(60) Lui, C. H.; Ye, Z.; Keiser, C.; Xiao, X.; He, R. Temperature-Activated Layer-Breathing Vibrations in Few-Layer Graphene. *Nano Lett.* **2014**, *14*, 4615−4621.

(61) Zhang, X.; Han, W.; Wu, J.; Milana, S.; Lu, Y.; Li, Q.; Ferrari, A.; Tan, P. Raman Spectroscopy of Shear and Layer Breathing Modes in Multilayer MoS_2. *Phys. Rev. B: Condens. Matter Mater. Phys.* **2013**, *87*, 115413.

(62) Zeng, H.; Zhu, B.; Liu, K.; Fan, J.; Cui, X.; Zhang, Q. Low-Frequency Raman Modes and Electronic Excitations in Atomically Thin MoS_2 Films. *Phys. Rev. B: Condens. Matter Mater. Phys.* **2012**, *86*, 241301.

(63) Boukhicha, M.; Calandra, M.; Measson, M.-A.; Lancry, O.; Shukla, A. Anharmonic Phonons in Few-Layer MoS_2: Raman Spectroscopy of Ultralow Energy Compression and Shear Modes. *Phys. Rev. B: Condens. Matter Mater. Phys.* **2013**, *87*, 195316.

(64) Zhao, Y.; Luo, X.; Li, H.; Zhang, J.; Araujo, P. T.; Gan, C. K.; Wu, J.; Zhang, H.; Quek, S. Y.; Dresselhaus, M. S.; Xiong, Q. Interlayer Breathing and Shear Modes in Few-Trilayer MoS_2 and WSe_2. *Nano Lett.* **2013**, *13*, 1007−1015.

(65) Luo, X.; Lu, X.; Koon, G. K. W.; Castro Neto, A. H.; Özyilmaz, B.; Xiong, Q.; Quek, S. Y. Large Frequency Change with Thickness in Interlayer Breathing Mode-Significant Interlayer Interactions in Few Layer Black Phosphorus. *Nano Lett.* **2015**, *15*, 3931−3938.

(66) Dong, S.; Zhang, A.; Liu, K.; Ji, J.; Ye, Y. G.; Luo, X. G.; Chen, X. H.; Ma, X.; Jie, Y.; Chen, C.; Wang, X.; Zhang, Q. Ultralow-Frequency Collective Compression Mode and Strong Interlayer Coupling in Multilayer Black Phosphorus. *Phys. Rev. Lett.* **2016**, *116*, 087401.

(67) Zhao, H.; Wu, J.; Zhong, H.; Guo, Q.; Wang, X.; Xia, F.; Yang, L.; Tan, P.; Wang, H. Interlayer Interactions in Anisotropic Atomically Thin Rhenium Diselenide. *Nano Res.* **2015**, *8*, 3651−3661.

(68) Nagler, P.; Plechinger, G.; Schuller, C.; Korn, T. Observation of Anisotropic Interlayer Raman Modes in Few-Layer ReS_2. *Phys. Status Solidi RRL* **2016**, *10*, 185−189.

(69) Zhao, Y.; Luo, X.; Zhang, J.; Wu, J.; Bai, X.; Wang, M.; Jia, J.; Peng, H.; Liu, Z.; Quek, S. Y.; Xiong, Q. Interlayer Vibrational Modes in Few-Quintuple-Layer Bi_2Te_3 and Bi_2Se_3 Two-Dimensional Crystals: Raman Spectroscopy and First-Principles Studies. *Phys. Rev. B: Condens. Matter Mater. Phys.* **2014**, *90*, 245428.

(70) Xi, X.; Zhao, L.; Wang, Z.; Berger, H.; Forr, L.; Shan, J.; Mak, K. F. Strongly Enhanced Charge-Density-Wave Order in Monolayer $NbSe_2$. *Nat. Nanotechnol.* **2015**, *10*, 765−769.

(71) He, R.; van Baren, J.; Yan, J.-A.; Xi, X.; Ye, Z.; Ye, G.; Lu, I.-H.; Leong, S.; Lui, C. Interlayer Breathing and Shear Modes in $NbSe_2$ Atomic Layers. *2D Mater.* **2016**, *3*, 031008.

(72) Stenger, I.; Schue, L.; Boukhicha, M.; Bérini, B.; Placais, B.; Loiseau, A.; Barjon, J. Low Frequency Raman Spectroscopy of Few-Atomic-Layer Thick hBN Crystals. *2D Mater.* **2017**, *4*, 031003.

(73) Lui, C. H.; Ye, Z.; Keiser, C.; Barros, E. B.; He, R. Stacking-Dependent Shear Modes in Trilayer Graphene. *Appl. Phys. Lett.* **2015**, *106*, 041904.

(74) Zhang, X.; Han, W.-P.; Qiao, X.-F.; Tan, Q.-H.; Wang, Y.-F.; Zhang, J.; Tan, P.-H. Raman Characterization of AB-and ABC-Stacked Few-Layer Graphene by Interlayer Shear Modes. *Carbon* **2016**, *99*, 118−122.

(75) Lu, X.; Utama, M.; Lin, J.; Luo, X.; Zhao, Y.; Zhang, J.; Pantelides, S. T.; Zhou, W.; Quek, S. Y.; Xiong, Q. Rapid and Nondestructive Identification of Polytypism and Stacking Sequences in Few-Layer Molybdenum Diselenide by Raman Spectroscopy. *Adv. Mater.* **2015**, *27*, 4502−4508.

(76) Yan, J.; Xia, J.; Wang, X.; Liu, L.; Kuo, J.-L.; Tay, B. K.; Chen, S.; Zhou, W.; Liu, Z.; Shen, Z. X. Stacking-Dependent Interlayer Coupling in Trilayer MoS_2 with Broken Inversion Symmetry. *Nano Lett.* **2015**, *15*, 8155−8161.

(77) O'Brien, M.; McEvoy, N.; Hanlon, D.; Hallam, T.; Coleman, J. N.; Duesberg, G. S. Mapping of Low-Frequency Raman Modes in CVD-Grown Transition Metal Dichalcogenides: Layer Number, Stacking Orientation and Resonant Effects. *Sci. Rep.* **2016**, *6*, 19476.

(78) Lee, J.-U.; Kim, K.; Han, S.; Ryu, G. H.; Lee, Z.; Cheong, H. Raman Signatures of Polytypism in Molybdenum Disulfide. *ACS Nano* **2016**, *10*, 1948−1953.

(79) Qiao, X.-F.; Wu, J.-B.; Zhou, L.; Qiao, J.; Shi, W.; Chen, T.; Zhang, X.; Zhang, J.; Ji, W.; Tan, P.-H. Polytypism and Unexpected Strong Interlayer Coupling in Two-Dimensional Layered ReS_2. *Nanoscale* **2016**, *8*, 8324−8332.

(80) He, R.; Yan, J.-A.; Yin, Z.; Ye, Z.; Ye, G.; Cheng, J.; Li, J.; Lui, C. H. Coupling and Stacking Order of ReS_2 Atomic Layers Revealed by Ultralow-Frequency Raman Spectroscopy. *Nano Lett.* **2016**, *16*, 1404−1409.

(81) Liang, L.; Puretzky, A. A.; Sumpter, B. G.; Meunier, V. Interlayer Bond Polarizability Model for Stacking-Dependent Low-Frequency Raman Scattering in Layered Materials. *Nanoscale* **2017**, *9*, 15340−15355.

(82) Cong, C.; Yu, T. Enhanced Ultra-Low-Frequency Interlayer Shear Modes in Folded Graphene Layers. *Nat. Commun.* **2014**, *5*, 4709.

(83) Wu, J. B.; Hu, Z. X.; Zhang, X.; Han, W. P.; Lu, Y.; Shi, W.; Qiao, X. F.; Ijas, M.; Milana, S.; Ji, W.; Ferrari, A. C.; Tan, P. H. Interface Coupling in Twisted Multilayer Graphene by Resonant Raman Spectroscopy of Layer Breathing Modes. *ACS Nano* **2015**, *9*, 7440−7449.

(84) Puretzky, A. A.; Liang, L.; Li, X.; Xiao, K.; Sumpter, B. G.; Meunier, V.; Geohegan, D. B. Twisted $MoSe_2$ Bilayers with Variable Local Stacking and Interlayer Coupling Revealed by Low-Frequency Raman Spectroscopy. *ACS Nano* **2016**, *10*, 2736−2744.

(85) Huang, S.; Liang, L.; Ling, X.; Puretzky, A. A.; Geohegan, D. B.; Sumpter, B. G.; Kong, J.; Meunier, V.; Dresselhaus, M. S. Low-Frequency Interlayer Raman Modes to Probe Interface of Twisted Bilayer MoS_2. *Nano Lett.* **2016**, *16*, 1435−1444.

(86) Lui, C. H.; Ye, Z.; Ji, C.; Chiu, K.-C.; Chou, C.-T.; Andersen, T. I.; Means-Shively, C.; Anderson, H.; Wu, J.-M.; Kidd, T.; Lee, Y.-H.; He, R. Observation of Interlayer Phonon Modes in van der Waals Heterostructures. *Phys. Rev. B: Condens. Matter Mater. Phys.* **2015**, *91*, 165403.

(87) Zhang, J.; Wang, J.; Chen, P.; Sun, Y.; Wu, S.; Jia, Z.; Lu, X.; Yu, H.; Chen, W.; Zhu, J.; Xie, G.; Yang, R.; Shi, D.; Xu, X.; Xiang, J.; Liu, K.; Zhang, G. Observation of Strong Interlayer Coupling in MoS_2/WS_2 Heterostructures. *Adv. Mater.* **2016**, *28*, 1950−1956.

(88) Verble, J.; Wieting, T. Lattice Mode Degeneracy in MoS_2 and Other Layer Compounds. *Phys. Rev. Lett.* **1970**, *25*, 362.

(89) Luo, X.; Zhao, Y.; Zhang, J.; Toh, M.; Kloc, C.; Xiong, Q.; Quek, S. Y. Effects of Lower Symmetry and Dimensionality on Raman Spectra in Two-Dimensional WSe_2. *Phys. Rev. B: Condens. Matter Mater. Phys.* **2013**, *88*, 195313.

(90) Damen, T. C.; Porto, S. P. S.; Tell, B. Raman Effect in Zinc Oxide. *Phys. Rev.* **1966**, *142*, 570−574.

(91) Zhang, J.; Peng, Z.; Soni, A.; Zhao, Y.; Xiong, Y.; Peng, B.; Wang, J.; Dresselhaus, M. S.; Xiong, Q. Raman Spectroscopy of Few-Quintuple Layer Topological Insulator Bi_2Se_3 Nanoplatelets. *Nano Lett.* **2011**, *11*, 2407−2414.

(92) Liang, L.; Meunier, V. First-Principles Raman Spectra of MoS_2, WS_2 and Their Heterostructures. *Nanoscale* **2014**, *6*, 5394.

(93) Wieting, T. Long-Wavelength Lattice Vibrations of MoS_2 and GaSe. *Solid State Commun.* **1973**, *12*, 931−935.

(94) Luo, X.; Lu, X.; Cong, C.; Yu, T.; Xiong, Q.; Quek, S. Y. Stacking Sequence Determines Raman Intensities of Observed Interlayer Shear Modes in 2D Layered Materials-a General Bond Polarizability Model. *Sci. Rep.* **2015**, *5*, 14565.

(95) Li, X.-L.; Qiao, X.-F.; Han, W.-P.; Zhang, X.; Tan, Q.-H.; Chen, T.; Tan, P.-H. Determining Layer Number of Two-Dimensional Flakes of Transition-Metal Dichalcogenides by the Raman Intensity from Substrates. *Nanotechnology* **2016**, *27*, 145704.

(96) Song, Q. J.; Tan, Q. H.; Zhang, X.; Wu, J. B.; Sheng, B. W.; Wan, Y.; Wang, X. Q.; Dai, L.; Tan, P. H. Physical Origin of Davydov Splitting and Resonant Raman Spectroscopy of Davydov Components in Multilayer $MoTe_2$. *Phys. Rev. B: Condens. Matter Mater. Phys.* **2016**, *93*, 115409.

(97) Froehlicher, G.; Lorchat, E.; Fernique, F.; Joshi, C.; Molina-Snchez, A.; Wirtz, L.; Berciaud, S. Unified Description of the Optical Phonon Modes in N-Layer $MoTe_2$. *Nano Lett.* **2015**, *15*, 6481−6489.

(98) Lorchat, E.; Froehlicher, G.; Berciaud, S. Splitting of Interlayer Shear Modes and Photon Energy Dependent Anisotropic Raman Response in N-Layer $ReSe_2$ and ReS_2. *ACS Nano* **2016**, *10*, 2752−2760.

(99) Qiao, X.-F.; Li, X.-L.; Zhang, X.; Shi, W.; Wu, J.-B.; Chen, T.; Tan, P.-H. Substrate-Free Layer-Number Identification of Two-Dimensional Materials: a Case of $Mo_{0.5}W_{0.5}S_2$ Alloy. *Appl. Phys. Lett.* **2015**, *106*, 223102.

(100) Glebov, A. L.; Mokhun, O.; Rapaport, A.; Vergnole, S.; Smirnov, V.; Glebov, L. B. Volume Bragg Gratings As Ultra-Narrow and Multiband Optical Filters. *Proc. SPIE* **2012**, 84280C.

(101) Miscuglio, M.; Lin, M.-L.; Di Stasio, F.; Tan, P.-H.; Krahne, R. Confined Acoustic Phonons in Colloidal Nanorod Heterostructures Investigated by Nonresonant Raman Spectroscopy and Finite Elements Simulations. *Nano Lett.* **2016**, *16*, 7664−7670.

(102) Mork, A. J.; Lee, E. M. Y.; Tisdale, W. A. Temperature Dependence of Acoustic Vibrations of CdSe and CdSe-CdS Core-Shell Nanocrystals Measured by Low-Frequency Raman Spectroscopy. *Phys. Chem. Chem. Phys.* **2016**, *18*, 28797−28801.

(103) Liu, X.-L.; Liu, H.-N.; Wu, J.-B.; Wu, H.-X.; Zhang, T.; Zhao, W.-Q.; Tan, P.-H. Filter-Based Ultralow-Frequency Raman Measurement down to 2 cm^{-1} for Fast Brillouin Spectroscopy Measurement. *Rev. Sci. Instrum.* **2017**, *88*, 053110.

(104) Lin, M.-L.; Ran, F.-R.; Qiao, X.-F.; Wu, J.-B.; Shi, W.; Zhang, Z.-H.; Xu, X.-Z.; Liu, K.-H.; Li, H.; Tan, P.-H. Ultralow-Frequency Raman System down to 10 cm^{-1} with Longpass Edge Filters and Its Application to the Interface Coupling in t(2 + 2)LGs. *Rev. Sci. Instrum.* **2016**, *87*, 053122.

(105) Zhao, W.; Ghorannevis, Z.; Chu, L.; Toh, M.; Kloc, C.; Tan, P.-H.; Eda, G. Evolution of Electronic Structure in Atomically Thin Sheets of WS_2 and WSe_2. *ACS Nano* **2013**, *7*, 791−797.

(106) Cao, T.; Wang, G.; Han, W.; Ye, H.; Zhu, C.; Shi, J.; Niu, Q.; Tan, P.; Wang, E.; Liu, B. Valley-Selective Circular Dichroism of Monolayer Molybdenum Disulphide. *Nat. Commun.* **2012**, *3*, 887.

(107) Han, C. Q.; Yao, M. Y.; Bai, X. X.; Miao, L.; Zhu, F.; Guan, D. D.; Wang, S.; Gao, C. L.; Liu, C.; Qian, D.; Liu, Y.; Jia, J.-f. Electronic Structure of Black Phosphorus Studied by Angle-Resolved Photoemission Spectroscopy. *Phys. Rev. B: Condens. Matter Mater. Phys.* **2014**, *90*, 085101.

(108) Li, L.; Kim, J.; Jin, C.; Ye, G. J.; Qiu, D. Y.; Jornada, F. H. D.; Shi, Z.; Chen, L.; Zhang, Z.; Yang, F.; et al. Direct Observation of the Layer-Dependent Electronic Structure in Phosphorene. *Nat. Nanotechnol.* **2016**, *12*, 21−25.

(109) Ni, Z. H.; Wang, H. M.; Kasim, J.; Fan, H. M.; Yu, T.; Wu, Y. H.; Feng, Y. P.; Shen, Z. X. Graphene Thickness Determination Using Reflection and Contrast Spectroscopy. *Nano Lett.* **2007**, *7*, 2758−2763.

(110) Jung, I.; Pelton, M.; Piner, R.; Dikin, D. A.; Stankovich, S.; Watcharotone, S.; Hausner, M.; Ruoff, R. S. Simple Approach for High-Contrast Optical Imaging and Characterization of Graphene-Based Sheets. *Nano Lett.* **2007**, *7*, 3569−3575.

(111) Li, H.; Wu, J.; Huang, X.; Lu, G.; Yang, J.; Lu, X.; Xiong, Q.; Zhang, H. Rapid and Reliable Thickness Identification of Two-Dimensional Nanosheets Using Optical Microscopy. *ACS Nano* **2013**, *7*, 10344−10353.

(112) Zhao, W.; Tan, P.; Zhang, J.; Liu, J. Charge Transfer and Optical Phonon Mixing in Few-Layer Graphene Chemically Doped with Sulfuric Acid. *Phys. Rev. B: Condens. Matter Mater. Phys.* **2010**, *82*, 245423.

(113) Cong, C.; Yu, T.; Sato, K.; Shang, J.; Saito, R.; Dresselhaus, G. F.; Dresselhaus, M. S. Raman Characterization of ABA-and ABC-Stacked Trilayer Graphene. *ACS Nano* **2011**, *5*, 8760−8768.

(114) Li, H.; Zhang, Q.; Yap, C. C. R.; Tay, B. K.; Edwin, T. H. T.; Olivier, A.; Baillargeat, D. From Bulk to Monolayer MoS_2: Evolution of Raman Scattering. *Adv. Funct. Mater.* **2012**, *22*, 1385−1390.

(115) Casiraghi, C.; Hartschuh, A.; Lidorikis, E.; Qian, H.; Harutyunyan, H.; Gokus, T.; Novoselov, K. S.; Ferrari, A. C. Rayleigh Imaging of Graphene and Graphene Layers. *Nano Lett.* **2007**, *7*, 2711−2717.

(116) Bosak, A.; Krisch, M.; Mohr, M.; Maultzsch, J.; Thomsen, C. Elasticity of Single-Crystalline Graphite: Inelastic X-Ray Scattering Study. *Phys. Rev. B: Condens. Matter Mater. Phys.* **2007**, *75*, 153408.

(117) Nicklow, R.; Wakabayashi, N.; Smith, H. Lattice Dynamics of Pyrolytic Graphite. *Phys. Rev. B* **1972**, *5*, 4951.

(118) Dolling, G.; Brockhouse, B. Lattice Vibrations in Pyrolitic Graphite. *Phys. Rev.* **1962**, *128*, 1120.

(119) Wakabayashi, N.; Smith, H.; Nicklow, R. Lattice Dynamics of Hexagonal MoS_2 Studied by Neutron Scattering. *Phys. Rev. B* **1975**, *12*, 659.

(120) Serrano, J.; Bosak, A.; Arenal, R.; Krisch, M.; Watanabe, K.; Taniguchi, T.; Kanda, H.; Rubio, A.; Wirtz, L. Vibrational Properties of Hexagonal Boron Nitride: Inelastic X-Ray Scattering and Ab Initio Calculations. *Phys. Rev. Lett.* **2007**, *98*, 095503.

(121) Fujii, Y.; Akahama, Y.; Endo, S.; Narita, S.; Yamada, Y.; Shirane, G. Inelastic Neutron Scattering Study of Acoustic Phonons of Black Phosphorus. *Solid State Commun.* **1982**, *44*, 579−582.

(122) Yamada, Y.; Fujii, Y.; Akahama, Y.; Endo, S.; Narita, S.; Axe, J.; McWhan, D. Lattice-Dynamical Properties of Black Phosphorus Under Pressure Studied by Inelastic Neutron Scattering. *Phys. Rev. B: Condens. Matter Mater. Phys.* **1984**, *30*, 2410.

(123) Feldman, J. Erratum For: Elastic Constants of 2H-MoS_2 and 2H-$NbSe_2$ Extracted from Measured Dispersion Curves and Linear Compressibilities. *J. Phys. Chem. Solids* **1981**, *42*, 1029.

(124) Tonndorf, P.; Schmidt, R.; Böttger, P.; Zhang, X.; Börner, J.; Liebig, A.; Albrecht, M.; Kloc, C.; Gordan, O.; Zahn, D. R. T.; de Vasconcellos, S. M.; Bratschitsch, R. Photoluminescence Emission and Raman Response of Monolayer MoS_2, $MoSe_2$, and WSe_2. *Opt. Express* **2013**, *21*, 4908−4916.

(125) Staiger, M.; Gillen, R.; Scheuschner, N.; Ochedowski, O.; Kampmann, F.; Schleberger, M.; Thomsen, C.; Maultzsch, J. Splitting of Monolayer Out-Of-Plane A_1' Raman Mode in Few-Layer WS_2. *Phys. Rev. B: Condens. Matter Mater. Phys.* **2015**, *91*, 195419.

(126) Phaneuf-L'Heureux, A.-L.; Favron, A.; Germain, J.-F.; Lavoie, P.; Desjardins, P.; Leonelli, R.; Martel, R.; Francoeur, S. Polarization-Resolved Raman Study of Bulk-like and Davydov-Induced Vibrational Modes of Exfoliated Black Phosphorus. *Nano Lett.* **2016**, *16*, 7761−7767.

(127) Kim, K.; Lee, J.-U.; Nam, D.; Cheong, H. Davydov Splitting and Excitonic Resonance Effects in Raman Spectra of Few-Layer $MoSe_2$. *ACS Nano* **2016**, *10*, 8113−8120.

(128) Miranda, H. P. C.; Reichardt, S.; Froehlicher, G.; Molina-Snchez, A.; Berciaud, S.; Wirtz, L. Quantum Interference Effects in Resonant Raman Spectroscopy of Single- and Triple-Layer $MoTe_2$ from First-Principles. *Nano Lett.* **2017**, *17*, 2381−2388.

(129) Grzeszczyk, M.; Goasa, K.; Zinkiewicz, M.; Nogajewski, K.; Molas, M. R.; Potemski, M.; Wysmoek, A.; Babiski, A. Layer-Number Dependent High-Frequency Vibration Modes in Few-Layer Transition Metal Dichalcogenides Induced by Interlayer Couplings. *2D Mater.* **2016**, *3*, 025010.

(130) Tan, Q.-H.; Sun, Y.-J.; Liu, X.-L.; Zhao, Y.; Xiong, Q.; Tan, P.-H.; Zhang, J. Observation of Forbidden Phonons, Fano Resonance and Dark Excitons by Resonance Raman Scattering in Few-Layer WS_2. *2D Mater.* **2017**, *4*, 031007.

(131) Tan, Q.-H.; Zhang, X.; Luo, X.-D.; Zhang, J.; Tan, P.-H. Layer-Number Dependent High-Frequency Vibration Modes in Few-Layer Transition Metal Dichalcogenides Induced by Interlayer Couplings. *J. Semicond.* **2017**, *38*, 031006.

(132) Chen, S.-Y.; Zheng, C.; Fuhrer, M. S.; Yan, J. Helicity-Resolved Raman Scattering of MoS_2, $MoSe_2$, WS_2, and WSe_2 Atomic Layers. *Nano Lett.* **2015**, *15*, 2526−2532.

(133) Soto, F.; Berger, H.; Cabo, L.; Carballeira, C.; Mosqueira, J.; Pavuna, D.; Toimil, P.; Vidal, F. Electric and Magnetic Characterization of $NbSe_2$ Single Crystals: Anisotropic Superconducting Fluctuations Above T_C. *Phys. C* **2007**, *460462*, 789−790.

(134) Wilson, J. A.; Salvo, F. J. D.; Mahajan, S. Charge-Density Waves and Superlattices in the Metallic Layered Transition Metal Dichalcogenides. *Adv. Phys.* **2001**, *50*, 1171−1248.

(135) Frindt, R. F. Superconductivity in Ultrathin $NbSe_2$ Layers. *Phys. Rev. Lett.* **1972**, *28*, 299−301.

(136) Staley, N. E.; Wu, J.; Eklund, P.; Liu, Y.; Li, L.; Xu, Z. Electric Field Effect on Superconductivity in Atomically Thin Flakes of $NbSe_2$. *Phys. Rev. B: Condens. Matter Mater. Phys.* **2009**, *80*, 184505.

(137) Hu, Z.-X.; Kong, X.; Qiao, J.; Normand, B.; Ji, W. Interlayer Electronic Hybridization Leads to Exceptional Thickness-Dependent Vibrational Properties in Few-Layer Black Phosphorus. *Nanoscale* **2016**, *8*, 2740−2750.

(138) Zhao, Y.; Qiao, J.; Yu, P.; Hu, Z.; Lin, Z.; Lau, S. P.; Liu, Z.; Ji, W.; Chai, Y. Extraordinarily Strong Interlayer Interaction in 2D Layered PtS_2. *Adv. Mater.* **2016**, *28*, 2399−2407.

(139) Zhao, Y.; Qiao, J.; Yu, Z.; Yu, P.; Xu, K.; Lau, S. P.; Zhou, W.; Liu, Z.; Wang, X.; Ji, W.; Chai, Y. High-Electron-Mobility and Air-Stable 2D Layered $PtSe_2$ FETs. *Adv. Mater.* **2017**, *29*, 1604230.

(140) Carozo, V.; Almeida, C. M.; Ferreira, E. H.; Cancado, L. G.; Achete, C. A.; Jorio, A. Raman Signature of Graphene Superlattices. *Nano Lett.* **2011**, *11*, 4527−4534.

(141) Kim, K.; Coh, S.; Tan, L. Z.; Regan, W.; Yuk, J. M.; Chatterjee, E.; Crommie, M.; Cohen, M. L.; Louie, S. G.; Zettl, A. Raman Spectroscopy Study of Rotated Double-Layer Graphene: Misorientation-Angle Dependence of Electronic Structure. *Phys. Rev. Lett.* **2012**, *108*, 246103.

(142) Craciun, M.; Russo, S.; Yamamoto, M.; Oostinga, J. B.; Morpurgo, A.; Tarucha, S. Trilayer Graphene Is a Semimetal with a Gate-Tunable Band Overlap. *Nat. Nanotechnol.* **2009**, *4*, 383−388.

(143) Xiao, D.; Liu, G.-B.; Feng, W.; Xu, X.; Yao, W. Coupled Spin and Valley Physics in Monolayers of MoS_2 and Other group-VI Dichalcogenides. *Phys. Rev. Lett.* **2012**, *108*, 196802.

(144) Xu, X.; Yao, W.; Xiao, D.; Heinz, T. F. Spin and Pseudospins in Layered Transition Metal Dichalcogenides. *Nat. Phys.* **2014**, *10*, 343−350.

(145) Mak, K. F.; He, K.; Shan, J.; Heinz, T. F. Control of Valley Polarization in Monolayer MoS_2 by Optical Helicity. *Nat. Nanotechnol.* **2012**, *7*, 494−498.

(146) Wu, W.; Wang, L.; Li, Y.; Zhang, F.; Lin, L.; Niu, S.; Chenet, D.; Zhang, X.; Hao, Y.; Heinz, T. F.; Hone, J.; Wang, Z. L. Piezoelectricity of Single-Atomic-Layer MoS_2 for Energy Conversion and Piezotronics. *Nature* **2014**, *514*, 470−474.

(147) Zhu, H.; Wang, Y.; Xiao, J.; Liu, M.; Xiong, S.; Wong, Z. J.; Ye, Z.; Ye, Y.; Yin, X.; Zhang, X. Observation of Piezoelectricity in Free-Standing Monolayer MoS_2. *Nat. Nanotechnol.* **2015**, *10*, 151−155.

(148) Xia, M.; Li, B.; Yin, K.; Capellini, G.; Niu, G.; Gong, Y.; Zhou, W.; Ajayan, P. M.; Xie, Y.-H. Spectroscopic Signatures of AA′ and AB Stacking of Chemical Vapor Deposited Bilayer MoS_2. *ACS Nano* **2015**, *9*, 12246−12254.

(149) Yan, A.; Chen, W.; Ophus, C.; Ciston, J.; Lin, Y.; Persson, K.; Zettl, A. Identifying Different Stacking Sequences in Few-Layer CVD-Grown MoS_2 by Low-Energy Atomic-Resolution Scanning Transmission Electron Microscopy. *Phys. Rev. B: Condens. Matter Mater. Phys.* **2016**, *93*, 041420.

(150) He, J.; Hummer, K.; Franchini, C. Stacking Effects on the Electronic and Optical Properties of Bilayer Transition Metal Dichalcogenides MoS_2, $MoSe_2$, WS_2, and WSe_2. *Phys. Rev. B: Condens. Matter Mater. Phys.* **2014**, *89*, 075409.

(151) Constantinescu, G.; Kuc, A.; Heine, T. Stacking in Bulk and Bilayer Hexagonal Boron Nitride. *Phys. Rev. Lett.* **2013**, *111*, 036104.

(152) Kuhn, A.; Chevy, A.; Chevalier, R. Crystal Structure and Interatomic Distances in GaSe. *Phys. Status Solidi A* **1975**, *31*, 469−475.

(153) Li, X.; Basile, L.; Yoon, M.; Ma, C.; Puretzky, A. A.; Lee, J.; Idrobo, J. C.; Chi, M.; Rouleau, C. M.; Geohegan, D. B.; Xiao, K. Revealing the Preferred Interlayer Orientations and Stackings of Two-Dimensional Bilayer Gallium Selenide Crystals. *Angew. Chem., Int. Ed.* **2015**, *54*, 2712−2717.

(154) Aroyo, M.; Perez-Mato, J.; Orobengoa, D.; Tasci, E.; De La Flor, G.; Kirov, A. Crystallography Online: Bilbao Crystallographic Server. *Bulg. Chem. Commun.* **2011**, *43*, 183−197.

(155) Umari, P.; Pasquarello, A.; Dal Corso, A. Raman Scattering Intensities in α-Quartz: A First-Principles Investigation. *Phys. Rev. B: Condens. Matter Mater. Phys.* **2001**, *63*, 094305.

(156) Lazzeri, M.; Mauri, F. First-Principles Calculation of Vibrational Raman Spectra in Large Systems: Signature of Small Rings in Crystalline SiO_2. *Phys. Rev. Lett.* **2003**, *90*, 036401.

(157) Snoke, D.; Cardona, M. A Bond Polarizability Model for the C60 Raman Spectrum. *Solid State Commun.* **1993**, *87*, 121−126.

(158) Guha, S.; Menendez, J.; Page, J.; Adams, G. Empirical Bond Polarizability Model for Fullerenes. *Phys. Rev. B: Condens. Matter Mater. Phys.* **1996**, *53*, 13106.

(159) Saito, R.; Furukawa, M.; Dresselhaus, G.; Dresselhaus, M. Raman Spectra of Graphene Ribbons. *J. Phys.: Condens. Matter* **2010**, *22*, 334203.

(160) Lin, J.; Liang, L.; Ling, X.; Zhang, S.; Mao, N.; Zhang, N.; Sumpter, B. G.; Meunier, V.; Tong, L.; Zhang, J. Enhanced Raman Scattering on In-Plane Anisotropic Layered Materials. *J. Am. Chem. Soc.* **2015**, *137*, 15511−15517.

(161) Ling, X.; Huang, S.; Hasdeo, E. H.; Liang, L.; Parkin, W. M.; Tatsumi, Y.; Nugraha, A. R. T.; Puretzky, A. A.; Das, P. M.; Sumpter, B. G.; Geohegan, D. B.; Kong, J.; Saito, R.; Drndic, M.; Meunier, V.; Dresselhaus, M. S. Anisotropic Electron-Photon and Electron-Phonon Interactions in Black Phosphorus. *Nano Lett.* **2016**, *16*, 2260−2267.

(162) Kim, J.; Lee, J.-U.; Lee, J.; Park, H. J.; Lee, Z.; Lee, C.; Cheong, H. Anomalous Polarization Dependence of Raman Scattering and Crystallographic Orientation of Black Phosphorus. *Nanoscale* **2015**, *7*, 18708−18715.

(163) Li, H.; Wu, J.-B.; Ran, F. R.; Lin, M.-L.; Liu, X.-L.; Zhao, Y. Y.; Lu, X.; Xiong, Q. H.; Zhang, J.; Huang, W.; Zhang, H.; Tan, P.-H. Interfacial Interactions in Van der Waals Heterostructures of MoS_2 and Graphene. *ACS Nano* **2017**, 10.1021/acsnano.7b07015.

(164) Wu, J.-B.; Wang, H.; Li, X.-L.; Peng, H.; Tan, P.-H. Raman Spectroscopic Characterization of Stacking Configuration and Interlayer Coupling of Twisted Multilayer Graphene Grown by Chemical Vapor Deposition. *Carbon* **2016**, *110*, 225−231.

(165) Lin, M.-L.; Chen, T.; Lu, W.; Tan, Q.-H.; Zhao, P.; Wang, H.-T.; Xu, Y.; Tan, P.-H. Identifying the Stacking Order of Multilayer Graphene Grown by Chemical Vapor Deposition Via Raman Spectroscopy. *J. Raman Spectrosc.* **2017**, DOI: 10.1002/jrs.5219.

(166) Lin, M.-L.; Wu, J.-B.; Liu, X.-L.; Tan, P.-H. Probing the Shear and Layer Breathing Modes in Multilayer Graphene by Raman Spectroscopy. *J. Raman Spectrosc.* **2017**, DOI: 10.1002/jrs.5224.

(167) Yan, W.; Liu, M.; Dou, R.-F.; Meng, L.; Feng, L.; Chu, Z.-D.; Zhang, Y.; Liu, Z.; Nie, J.-C.; He, L. Angle-Dependent van Hove Singularities in a Slightly Twisted Graphene Bilayer. *Phys. Rev. Lett.* **2012**, *109*, 126801.

(168) Luican, A.; Li, G.; Reina, A.; Kong, J.; Nair, R. R.; Novoselov, K. S.; Geim, A. K.; Andrei, E. Y. Single-Layer Behavior and Its Breakdown in Twisted Graphene Layers. *Phys. Rev. Lett.* **2011**, *106*, 126802.

(169) He, R.; Chung, T.-F.; Delaney, C.; Keiser, C.; Jauregui, L. A.; Shand, P. M.; Chancey, C. C.; Wang, Y.; Bao, J.; Chen, Y. P. Observation of Low Energy Raman Modes in Twisted Bilayer Graphene. *Nano Lett.* **2013**, *13*, 3594−3601.

(170) Huang, B.; Clark, G.; Navarro-Moratalla, E.; Klein, D. R.; Cheng, R.; Seyler, K. L.; Zhong, D.; Schmidgall, E.; McGuire, M. A.; Cobden, D. H.; Yao, W.; Xiao, D.; Jarillo-Herrero, P.; Xu, X. Layer-Dependent Ferromagnetism in a van der Waals Crystal down to the Monolayer Limit. *Nature* **2017**, *546*, 270−273.

(171) Gong, C.; Li, L.; Li, Z.; Ji, H.; Stern, A.; Xia, Y.; Cao, T.; Bao, W.; Wang, C.; Wang, Y.; Qiu, Z. Q.; Cava, R. J.; Louie, S. G.; Xia, J.; Zhang, X. Discovery of Intrinsic Ferromagnetism in Two-Dimensional van der Waals Crystals. *Nature* **2017**, *546*, 265−269.

(172) Zhong, D.; Seyler, K. L.; Linpeng, X.; Cheng, R.; Sivadas, N.; Huang, B.; Schmidgall, E.; Taniguchi, T.; Watanabe, K.; McGuire, M. A.; Yao, W.; Xiao, D.; Fu, K.-M. C.; Xu, X. Van der Waals Engineering of Ferromagnetic Semiconductor Heterostructures for Spin and Valleytronics. *Sci. Adv.* **2017**, *3*, e1603113.

(173) Bonini, N.; Lazzeri, M.; Marzari, N.; Mauri, F. Phonon Anharmonicities in Graphite and Graphene. *Phys. Rev. Lett.* **2007**, *99*, 176802.

(174) Paulatto, L.; Mauri, F.; Lazzeri, M. Anharmonic Properties from a Generalized Third-Order Ab Initio Approach: Theory and Applications to Graphite and Graphene. *Phys. Rev. B: Condens. Matter Mater. Phys.* **2013**, *87*, 214303.

(175) Soubelet, P.; Bruchhausen, A.; Fainstein, A.; Nogajewski, K.; Faugeras, C. Resonance Effects in the Raman Scattering of Monolayer and Few-Layer $MoSe_2$. *Phys. Rev. B: Condens. Matter Mater. Phys.* **2016**, *93*, 155407.

(176) del Corro, E.; Botello-Méndez, A.; Gillet, Y.; Elias, A. L.; Terrones, H.; Feng, S.; Fantini, C.; Rhodes, D.; Pradhan, N.; Balicas, L.; Gonze, X.; Charlier, J.-C.; Terrones, M.; Pimenta, M. A. Atypical Exciton-Phonon Interactions in WS_2 and WSe_2 Monolayers Revealed by Resonance Raman Spectroscopy. *Nano Lett.* **2016**, *16*, 2363−2368.

(177) Talirz, L.; Sode, H.; Dumslaff, T.; Wang, S.; Sanchez-Valencia, J. R.; Liu, J.; Shinde, P.; Pignedoli, C. A.; Liang, L.; Meunier, V.; Plumb, N. C.; Shi, M.; Feng, X.; Narita, A.; Mllen, K.; Fasel, R.; Ruffieux, P. On-Surface Synthesis and Characterization of 9-Atom Wide Armchair Graphene Nanoribbons. *ACS Nano* **2017**, *11*, 1380−1388.

(178) Profeta, M.; Mauri, F. Theory of Resonant Raman Scattering of Tetrahedral Amorphous Carbon. *Phys. Rev. B: Condens. Matter Mater. Phys.* **2001**, *63*, 245415.